Title: Parametric optimization and heat transfer analysis of a dual loop ORC (organic Rankine cycle) system for CNG engine waste heat recovery

First Author: Fubin Yang

Order of Authors: Fubin Yang[a,b], Hongguang Zhang[a,b,*], Zhibin Yu[c], Enhua Wang[c], Fanxiao Meng[a,b], Hongda Liu[a,b], Jingfu Wang[a,d]

Author's institution: [a] Beijing University of Technology. [b] Collaborative Innovation Center of Electric Vehicles in Beijing. [c] University of Glasgow. [d] Key Laboratory of Enhanced Heat Transfer and Energy Conservation, Ministry of Education.

***Corresponding author:** Professor Hongguang Zhang, PhD

Corresponding author's institution: Beijing University of Technology

Corresponding author's address: Pingleyuan No.100, 100124 Beijing, China. E-mail address: zhanghongguang@bjut.edu.cn, Tel.:+86 10 6739 2469; Fax: +86 10 6739 2774.

Parametric optimization and heat transfer analysis of a dual loop ORC (organic Rankine cycle) system for CNG engine waste heat recovery

Fubin Yang[a,b], Hongguang Zhang[a,b,*], Zhibin Yu[c], Enhua Wang[c], Fanxiao Meng[a,b], Hongda Liu[a,b], Jingfu Wang[a,d]

[a] College of Environmental and Energy Engineering, Beijing University of Technology, Pingleyuan No.100, 100124 Beijing, China

[b] Collaborative Innovation Center of Electric Vehicles in Beijing, Pingleyuan No.100, 100124 Beijing, China

[c] School of Engineering, University of Glasgow, Glasgow G12 8QQ, UK

[d] Key Laboratory of Enhanced Heat Transfer and Energy Conservation, Ministry of Education, Beijing University of Technology, Pingleyuan No.100, 100124 Beijing, China

Abstract: In this study, a dual loop ORC (organic Rankine cycle) system is adopted to recover exhaust energy, waste heat from the coolant system, and intercooler heat rejection of a six-cylinder CNG (compressed natural gas) engine. The thermodynamic, heat transfer, and optimization models for the dual loop ORC system are established. On the basis of the waste heat characteristics of the CNG engine over the whole operating range, a GA (genetic algorithm) is used to solve the Pareto solution for the thermodynamic and heat transfer performances to maximize net power output and minimize heat transfer area. Combined with optimization results, the optimal parameter regions of the dual loop ORC system are determined under various operating conditions. Then, the variation in the heat transfer area with the operating conditions of the CNG engine is analyzed. The results show

that the optimal evaporation pressure and superheat degree of the HT (high temperature) cycle are mainly influenced by the operating conditions of the CNG engine. The optimal evaporation pressure and superheat degree of the HT cycle over the whole operating range are within 2.5–2.9 MPa and 0.43–12.35 K, respectively. The optimal condensation temperature of the HT cycle, evaporation and condensation temperatures of the LT (low temperature) cycle, and exhaust temperature at the outlet of evaporator 1 are kept nearly constant under various operating conditions of the CNG engine. The thermal efficiency of the dual loop ORC system is within the range of 8.79%–10.17%. The dual loop ORC system achieves the maximum net power output of 23.62 kW under the engine rated condition. In addition, the operating conditions of the CNG engine and the operating parameters of the dual loop ORC system significantly influence the heat transfer areas for each heat exchanger.

Keywords: CNG engine; Waste heat recovery; Dual loop organic Rankine cycle; Parametric optimization; Heat transfer analysis

Nomenclature

$\dot{W}$	power (kW) or channel width (m)
$\dot{Q}$	heat transfer rate (kW)
$\dot{m}$	mass flow rate (kg/s)
h	specific enthalpy (kJ/kg) or convective heat transfer coefficient (W/m^2.K)
s	specific entropy (kJ/kg.K)
T	temperature (K)

P	pressure (MPa)
K	overall heat transfer coefficient ($W/m^2.K$)
A	heat transfer area (m^2)
Nu	Nusselt number
d	diameter (m)
r	fouling resistance ($m^2.K/W$)
Re	Reynolds number
Pr	Prandtl number
l	length (m)
c_t	temperature difference correction factor
f	resistance coefficient
F	forced convective heat transfer enhancement factor
S	suppression factor
x	quality
p_r	reduced pressure
q	heat flux (W/m^2)
M	molecular weight (kg/kmol)
i_{fg}	enthalpy of vaporization (J/kg)
q''_{wall}	imposed wall heat flux (W/m^2)
G	mass velocity ($kg/m^2.s$)
D	port diameter (m)

N	number
b	channel spacing (m)
Bo	boiling number
r_{bw}	back work ratio

Greek symbols

β	rib effect coefficient or chevron angle
α	heat transfer coefficient (W/m^2.K)
λ	thermal conductivity (W/m.K)
η	efficiency
δ	fin height (m)
ε	correction factor or effectiveness of the heat exchanger
ρ	density (kg/m^3)

Subscripts

exp1	expander1
H	high temperature
H1 – H7	state points in HT cycle
ise	isentropic
pre	preheater
p1	pump1

eva1	evaporator1
exh	exhaust
a – d	state points in exhaust gas
exp2	expander2
L	low temperature or all the mass flow rate taken as liquid
L1 – L8	state points in LT cycle
in	inner
out	outer
con	condenser
p2	pump2
int	intercooler
eva2	evaporator2
cool	coolant
tot	total
th	thermal
max	maximum
min	minimum
ft	fin-and-tube
wf	working fluid
l	liquid
v	vapor

tp	two-phase
fb	film boiling
nb	nucleate boiling
pla	plate
h	hydraulic
eq	equivalent
out	outlet

Acronyms

ORC	organic Rankine cycle
CNG	compressed natural gas
GA	genetic algorithm
HT	high temperature
LT	low temperature
IC	internal combustion
EGR	exhaust gas recirculation
ODP	ozone depletion potential
GWP	global warming potential
CFCs	chlorofluorocarbon
HCFCs	hydrochlorofluorocarbons
PPTD	pinch point temperature difference

LMTD	logarithmic mean temperature difference
BSFC	brake specific fuel consumption
TOPSIS	Technique for Order Preference by Similarity to an Ideal Solution
IHE	internal heat exchanger
WHRE	waste heat recovery efficiency

1. **Introduction**

As a primary power machine used in the transportation industry, IC (internal combustion) engines typically utilize fossil fuels. In recent years, environmental degradation caused by particulate emissions from IC engines has received extensive attention. Simultaneously, emission regulations are becoming progressively stricter to improve air quality. Clean alternative fuel is a good option for traditional IC engines. Among all types of alternative fuels, CNG (compressed natural gas) is considered one of the most promising options because of its low emission levels, low price, and abundant reserves [1]. In China, CNG engines have been widely used in buses, heavy-duty trucks, and power units. However, CNG engines also produce a large amount of waste heat while they are running. The thermal efficiency of an engine is difficult to improve markedly using existing technologies. Waste heat recovery technologies do not only enhance the energy utilization efficiency of IC engines, but also reduce hazard emissions [2].

ORC (organic Rankine cycle) technology has been widely studied for low grade waste heat recovery because of its simple configuration, high efficiency, and capability to operate efficiently under low and medium grade heat sources [3–6]. After the energy crisis of the 1970s, ORC technology has been gradually applied to the waste heat recovery of IC engines [7–9]. In recent years, an increasing number of scholars have focused on studying this promising field [10–16]. Vaja et al. conducted a thermodynamic analysis to efficiently recover the waste heat of a stationary IC engines. Three working fluids and cycle configurations were considered for the parametric and performance analyses of the ORC system. The results showed that a 12% increase in overall efficiency could be achieved compared with the engine alone [17]. Srinivasan et al. investigated the

exhaust waste heat recovery potential of a dual fuel combustion engine using a bottoming ORC system. Potential improvements in fuel conversion efficiency and brake specific emissions were quantified. The results showed that fuel conversion efficiency could be improved by an average of 7 percentage points via hot EGR (exhaust gas recirculation) and ORC turbocompounding [18]. Usman et al. evaluated the positive and negative effects of installing an ORC system in a light-duty vehicle. The results showed that if the negative effects were considered, the maximum power enhancement was 5.82% at a vehicle speed of 100 km/h [19].

A simple ORC configuration can only be used to recover the waste heat of a single heat source, which will result in a low power output and a high cost. The waste heat of an IC engine is released into the atmosphere through the exhaust gas and coolant. For IC engines equipped with a turbocharger, a fraction of waste heat is retained in the intercooler. Therefore, reasonable configurations should be developed for the cascade utilization of waste heat from IC engines [20-22]. Zhang et al. designed a dual loop ORC system to simultaneously recover waste heat from the exhaust gas, intake air, and coolant. The results showed that the relative output power improved from 14%–16% in the peak of the effective thermal efficiency region [23]. Shu et al. proposed a novel transcritical cascade-ORC system to recover multi-grade waste heat from a heavy-duty diesel engine. The comparison and screening of working fluids were also conducted for the high temperature and low temperature loops. The results showed that a maximum net power output of 38.2 kW could be achieved [24]. Song et al. investigated the waste heat recovery of a diesel engine using a dual loop ORC system. Parametric analysis was conducted to evaluate system performance. The results showed that the maximum net power output of the dual loop ORC system reaches 111.2

kW, compared with an increase of 11.2% in the original engine power [25].

Parametric optimization is an important method to improve ORC performance. The more complex the system configurations are, the more the parameters involve [26–28]. Wang et al. conducted a parametric analysis of a dual loop ORC system for the waste heat recovery of a diesel engine. The effects of three working parameters, namely, expander isentropic efficiency, evaporation pressure of the high temperature loop, and condensation temperature of the low temperature loop, on the performance of the dual loop ORC system were evaluated. The results showed that the effect of the evaporation pressure of the high temperature loop on the dual loop ORC system was weak. Moreover, the expander isentropic efficiency and condensation temperature of the low temperature loop were two important parameters for the dual loop ORC system [29]. Shu et al. proposed a dual loop ORC system to recover waste heat from the exhaust, engine coolant, and residual heat of the HT cycle. The effects of the working fluid, evaporation temperature of the high temperature and low temperature cycles, and the operating loads of the diesel engine on the net power output and exergy efficiency were analyzed. The results showed that the maximum net power output and exergy efficiency were 36.77 kW and 55.05%, respectively, with R1234yf as the working fluid [30].

As a heat transfer device between the waste heat source and the working fluid, the performance of a heat exchanger directly affects an ORC system. Wang et al. analyzed the thermal-hydraulic characteristics of a fin-and-tube evaporator for engine waste heat recovery using a CFD (computational fluid dynamics) method and the synergy principle. The flow and heat transfer mechanisms of the exhaust gas in the evaporator were investigated. The results showed that fin-and-tube evaporator was a feasible choice for engine waste heat recovery systems, and heat

transfer performance could be enhanced by optimizing the shapes and angles of the fins [31]. Imran et al. developed thermal and hydraulic design models for a chevron type plate evaporator, and optimized its geometrical parameters for a low temperature geometric ORC system. The main geometric parameters of the evaporator were selected as decision variables with minimum cost and pressure drop as the objective functions. The results showed that a range of optimum allowable pressure drops existed in the evaporator [32]. Bei et al. established a simulation model for a fin-and-tube evaporator for diesel engine waste heat recovery systems. The flow and heat transfer characteristics of the exhaust gas at the shell side were analyzed. The influence of the exhaust back pressure on the diesel engine was also studied. The results showed that the installation of the evaporator slightly affected on the diesel engine [33].

To our knowledge, the simple ORC system is widely used for waste heat recovery in IC engines. Increasing evaporation pressure and superheat degree does not only improve cycle efficiency, but also provides a convenient means of decreasing irreversible loss considering that temperature is relatively high. If the expander inlet state is maintained the same, then condensing the working fluid to lower temperatures is another means to increase net power output. However, lowering the condensation temperature is not without any negative effects. First, it increases the expansion ratio during the expansion process. A large expansion ratio is highly undesirable in small-power level ORC applications because this component has not yet reached technical maturity for large-scale industrialization [6]. Moreover, a large expansion ratio increases the possibility of the working fluid leaking into the atmosphere. Therefore, there is a lower limit on condensation temperature that can be used in practical applications. While condensing the working fluid to a moderate temperature,

part of the heat rejection is wasted in the condenser. The simple ORC system can only be used to recover waste heat from a single heat source. Apart from exhaust gas, the waste heat of the coolant and the turbocharged air in the intercooler are also worth recovering. Compared with that of exhaust gas, the temperatures of the coolant and turbocharged air are relatively low. The efficient and simultaneous recovery of these components is difficult because of the diversity and multi-grade characteristics of the waste heat sources of an IC engine. Therefore, a dual loop ORC system, which typically consists of two ORC loops, is proposed to improve the matching of multi-grade heat sources is proposed. The HT (high temperature) cycle is used to recover exhaust energy, whereas the LT (low temperature) cycle is designed to utilize the waste heat from the coolant system, the heat rejection from the intercooler, and the residual heat from the condensation process of the HT cycle. These two cycles are coupled through a preheater. As summarized above, the dual loop ORC system is a promising technology for multi-grade waste heat recovery in IC engine applications.

From the aforementioned discussions, the dual loop ORC system can be concluded as an effective means to realize cascade utilization of waste heat from IC engines. However, most current studies have focused only on the stationary heat source conditions and parameters sensitivity analysis, whereas only a few have considered multi-objective and multi-parameter optimization by using an evolutionary algorithm. In addition, an IC engine frequently operates under various operating conditions. Therefore, an important issue is determining how to deal with the coordinated variation between the operating parameters of the dual loop ORC system and the operating conditions of an IC engine. The main contribution of the present study is to identify the optimal operating regions of the ORC system by considering the thermodynamic performance and heat transfer characteristics

under various operating conditions of a CNG engine using a genetic algorithm. The same method can also be applied in other waste heat recovery systems. Furthermore, the heat exchanger contributes a large proportion to the total investment cost [34]. Analyzing the heat transfer characteristics of the heat exchangers is necessary to optimize the system configuration. In this study, the waste heat characteristics of a CNG engine are first investigated under various operating conditions. Subsequently, the thermodynamic, heat transfer and optimization models of the dual loop ORC system are established for a cascade utilization of engine waste heat. The evaporation pressure, superheat degree, and condensation temperature of the HT cycle, the evaporation and condensation temperatures of the LT cycle, and exhaust temperature at the outlet of evaporator are selected as decision variables for maximizing net power output and minimizing heat transfer area. The GA (genetic algorithm) is adopted to obtain the synergetic variation law for operating parameters of the dual loop ORC system under various conditions.

2. **Dual loop ORC system**

2.1. System description

The objective of this study is to recover the waste heat of a CNG engine using a dual loop ORC system. When the IC engine is running, the exhaust temperature is relatively high, whereas the coolant and intake air temperatures are relatively low. As shown in Fig. 1, the dual loop ORC system is designed based on the waste heat characteristics of the IC engine. The dual loop ORC system consists of an HT (high temperature) cycle and an LT (low temperature) cycle. The HT cycle is used to recover the exhaust energy, whereas the LT cycle is adopted to utilize the waste heat from the coolant system, intercooler heat rejection, and the released heat from the condensation process

of the HT cycle. In the HT cycle, the working fluid is pressurized into a high pressure state by pump 1. Then the working fluid absorbs exhaust waste heat in evaporator 1 and converts it into a high temperature and high pressure vapor state. Subsequently, the high temperature and high pressure vapor enters expander 1 to make it run, thereby causing generator 1 to produce electricity. Afterwards, the superheated and low pressure vapor exported from expander1 is condensed into a saturated liquid state after the heat transfer process in the preheater. The HT cycle completes one working cycle with this change. In the LT cycle, the working fluid is pressurized into a subcooled liquid state using pump 2. Subsequently, the working fluid is heated sequentially by the turbocharged air and the released heat from the condensation process of the HT cycle into a two-phase state. Later, the two-phase working fluid is transformed into a saturated vapor state after the endothermic process is completed in evaporator 2. The saturated vapor flows into expander 2, which causes it to run and to drive generator 2 to produce electricity. Finally, the superheated vapor exported from expander 2 condenses into a saturated liquid state in the condenser. In this manner, the entire process is completed.

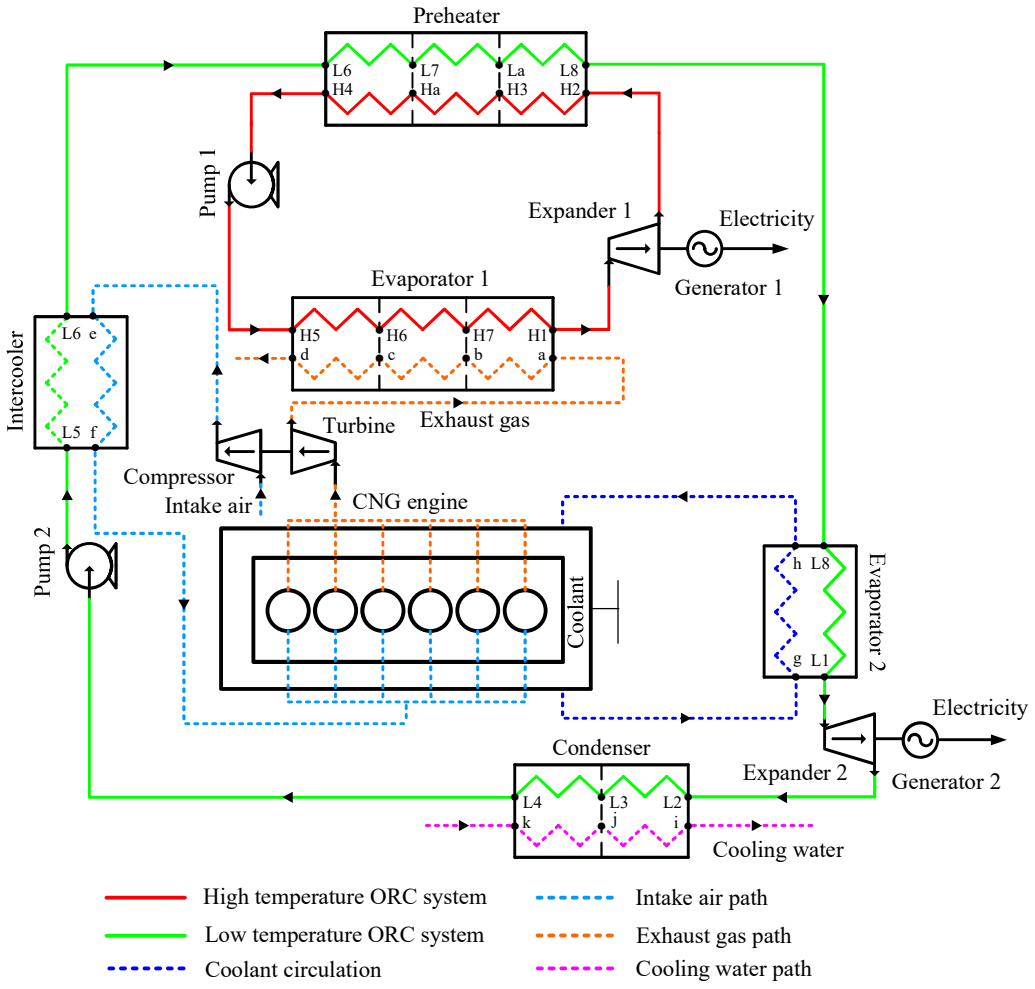

Fig. 1. Schematic diagram of the dual loop ORC system (various labels refer to thermodynamic analysis state points shown in Figs. 2 and 3).

2.2. Working fluid selection

After the system configuration is determined, the thermodynamic properties of the working fluid and other operating conditions strongly influence system performances. A suitable working fluid should fulfill the requirements of thermodynamic properties, environmental impacts, safety levels, and chemical stability. CFCs (chlorofluorocarbon) and HCFCs (hydrochlorofluorocarbons) are first excluded because of their high ODP (ozone depletion potential) and GWP (global warming potential). Dry or isentropic working fluids are generally preferred to prevent the presence of

droplets after the expansion process. Working fluids with a low critical temperature and pressure can easily enter the supercritical state after the endothermic process because of high exhaust temperatures. A supercritical cycle will increase the difficulty of the condensation process [35]. For practical applications, both cycles should use the same working fluid to reduce system complexity. Many scholars have indicated that R245fa performs better than other organic working fluids for the recovery of low grade waste heat when cycle performance is comprehensively considered [3,4,14,30,35,36]. Therefore, R245fa is selected as the working fluid for both cycles, and its properties are listed in Table 1. The effect of different working fluids on the dual loop ORC system will be discussed in the future works.

Table 1 Properties of R245fa.

Parameters	Values
Molecular formula	$CHF_2CH_2CF_3$
Molecular weight (kg/kmol)	134.05
Critical temperature (K)	427.16
Critical pressure (MPa)	3.65
Boiling temperature (K)	288.29
ASHRAE 34 safety group	B1
Atmospheric life time (yr)	7.2
ODP	0
GWP (100 yrs)	950

2.3. Thermodynamic modeling

The thermodynamic model for the dual loop ORC system is established based on the first and second laws of thermodynamics.

2.3.1. HT loop ORC process

The *T*–*s* diagram of the HT cycle is shown in Fig. 2.

Process H1–H2 (Expander):

The power output and isentropic efficiency of expander 1 can be expressed as:

$$\dot{W}_{\mathrm{exp1}} = \dot{m}_{\mathrm{H}}(h_{\mathrm{H1}} - h_{\mathrm{H2}}) \tag{1}$$

$$\eta_{\mathrm{ise,exp1}} = \frac{h_{\mathrm{H1}} - h_{\mathrm{H2}}}{h_{\mathrm{H1}} - h_{\mathrm{H2s}}} \tag{2}$$

Process H2–H4 (Preheater):

The heat transfer rate of the preheater can be determined as:

$$\dot{Q}_{\mathrm{H,pre}} = \dot{m}_{\mathrm{H}}(h_{\mathrm{H2}} - h_{\mathrm{H4}}) \tag{3}$$

Process H4–H5 (Pump 1):

The power consumed and isentropic efficiency of pump 1 can be expressed as:

$$\dot{W}_{\mathrm{p1}} = \dot{m}_{\mathrm{H}}(h_{\mathrm{H5}} - h_{\mathrm{H4}}) \tag{4}$$

$$\eta_{\mathrm{isep1}} = \frac{h_{\mathrm{H5s}} - h_{\mathrm{H4}}}{h_{\mathrm{H5}} - h_{\mathrm{H4}}} \tag{5}$$

Process H5–H1 (Evaporator 1):

The heat transfer rate of evaporator 1 is given by:

$$\dot{Q}_{\mathrm{eva1}} = \dot{m}_{\mathrm{H}}(h_{\mathrm{H1}} - h_{\mathrm{H5}}) = \dot{m}_{\mathrm{exh}}(h_{\mathrm{exh,a}} - h_{\mathrm{exh,d}}) \tag{6}$$

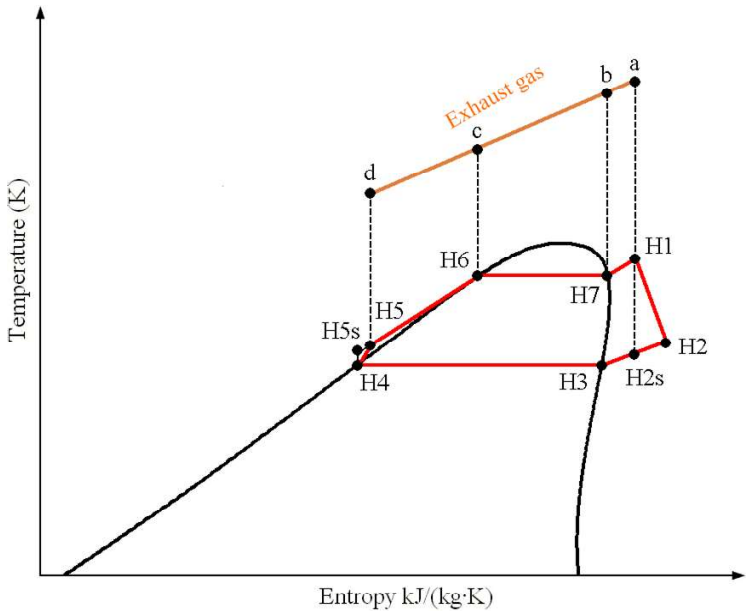

Fig. 2. *T*–*s* diagram of the HT loop ORC system.

2.3.2. LT loop ORC process

The *T*–*s* diagram of the LT cycle is presented in Fig. 3.

Process L1–L2 (Expander):

The power output and isentropic efficiency of expander 2 can be determined as:

$$\dot{W}_{\exp 2} = \dot{m}_{\mathrm{L}} (h_{\mathrm{L}1} - h_{\mathrm{L}2}) \tag{7}$$

$$\eta_{\mathrm{ise,exp}2} = \frac{h_{\mathrm{L}1} - h_{\mathrm{L}2}}{h_{\mathrm{L}1} - h_{\mathrm{L}2\mathrm{s}}} \tag{8}$$

Process L2–L4 (Condenser):

The heat transfer rate of the condenser can be expressed as:

$$\dot{Q}_{\mathrm{con}} = \dot{m}_{\mathrm{L}} (h_{\mathrm{L}2} - h_{\mathrm{L}4}) \tag{9}$$

Process L4–L5 (Pump):

The power consumed and isentropic efficiency of pump 2 can be determined as:

$$\dot{W}_{\mathrm{p}2} = \dot{m}_{\mathrm{L}} (h_{\mathrm{L}5} - h_{\mathrm{L}4}) \tag{10}$$

$$\eta_{\mathrm{ise,p}2} = \frac{h_{\mathrm{L}5\mathrm{s}} - h_{\mathrm{L}4}}{h_{\mathrm{L}5} - h_{\mathrm{L}4}} \tag{11}$$

Process L5–L6 (Intercooler):

The heat transfer rate of the intercooler can be expressed as:

$$\dot{Q}_{\mathrm{int}} = \dot{m}_{\mathrm{L}} (h_{\mathrm{L}6} - h_{\mathrm{L}5}) = \dot{m}_{\mathrm{air}} (h_{\mathrm{air,e}} - h_{\mathrm{air,f}}) \tag{12}$$

Process L6–L8 (Preheater):

The heat transfer rate of the preheater can be expressed as:

$$\dot{Q}_{\mathrm{L,pre}} = \dot{m}_{\mathrm{L}} (h_{\mathrm{L}8} - h_{\mathrm{L}6}) = \varepsilon_{\mathrm{pre}} \dot{Q}_{\mathrm{H,pre}} \tag{13}$$

Process L8–L1 (Evaporator 2):

The heat transfer rate of evaporator 2 can be determined as:

$$\dot{Q}_{\mathrm{eva2}} = \dot{m}_{\mathrm{L}}(h_{\mathrm{L1}} - h_{\mathrm{L8}}) = \varepsilon_{\mathrm{eva2}}\dot{m}_{\mathrm{cool}}(h_{\mathrm{coolg}} - h_{\mathrm{coolh}}) \quad (14)$$

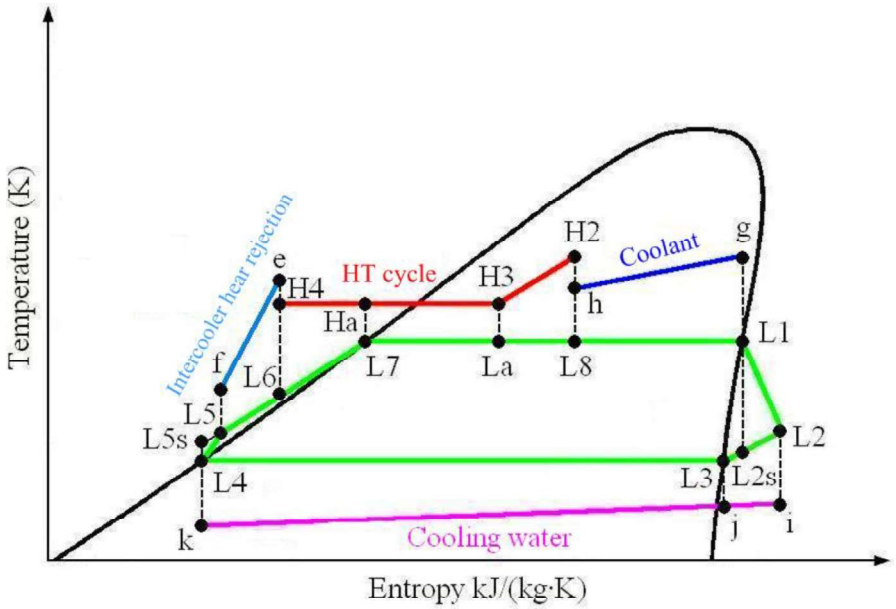

Fig. 3. *T*–*s* diagram of the LT loop ORC system.

2.3.3. Performance parameters and assumptions of the dual loop ORC system

The evaluation indicators of the ORC system mainly include net power output and thermal efficiency from the viewpoints of thermodynamics. The objective of performance optimization is to obtain a high net power output and thermal efficiency. Therefore, net power output and thermal efficiency are adopted to evaluate the thermodynamic performance of the dual loop ORC system in this study.

The net power output of the HT cycle can be calculated using the following equations:

$$\dot{W}_{\mathrm{H,net}} = \dot{W}_{\mathrm{exp1}} - \dot{W}_{\mathrm{p1}} \quad (15)$$

The net power output of the LT cycle can be expressed as:

$$\dot{W}_{\mathrm{L,net}} = \dot{W}_{\mathrm{exp2}} - \dot{W}_{\mathrm{p2}} \quad (16)$$

The total net power output of the dual loop ORC system can be determined as:

$$\dot{W}_{\mathrm{totnet}} = \dot{W}_{\mathrm{H,net}} - \dot{W}_{\mathrm{L,net}} \quad (17)$$

The thermal efficiency of the dual loop ORC system can be expressed as:

$$\eta_{\mathrm{th}} = \frac{\dot{W}_{\mathrm{tot,net}}}{\dot{Q}_{\mathrm{eva1}} + \dot{Q}_{\mathrm{int}} + \dot{Q}_{\mathrm{eva2}}} \tag{18}$$

For the dual loop ORC system, the following assumptions are made.

(1) The entire system operates under steady state conditions.

(2) No pressure drop occurs in the pipes and components.

(3) The isentropic efficiencies of the pump and the expander are set to 0.7 [3] and 0.65 [5], respectively.

(4) The effectiveness of the heat exchanger is set to 0.5 [17,37].

2.4. Heat exchanger modeling

As a coupling unit between the waste heat source and the ORC system, the heat exchanger significantly influences the overall performances of the ORC system. The waste heat characteristics of the exhaust gas, turbocharged air, and coolant vary with the operating conditions of the CNG engine. These characteristics will further affect heat transfer performance. Furthermore, the dual loop ORC system involves multiple heat exchangers and phase change processes. Therefore, analyzing the heat transfer process of the dual loop ORC system is necessary. The LMTD (logarithmic mean temperature difference) method is adopted to establish the heat transfer model. The heat transfer rate in each section can be expressed as:

$$\dot{Q} = KA\Delta T_{\mathrm{LMTD}} \tag{19}$$

The LMTD is given by:

$$\Delta T_{\mathrm{LMTD}} = \frac{\Delta t_{\max} - \Delta t_{\min}}{\ln \dfrac{\Delta t_{\max}}{\Delta t_{\min}}} \tag{20}$$

When selecting the heat exchangers for dual loop ORC system, the distribution characteristics of the waste heat source should be considered. The exhaust temperature is relatively high based on the waste heat characteristics of the IC engine [38]. The evaporator of the HT cycle should use a heat exchanger that is suitable for complicated conditions. Compared with shell-and-tube heat exchangers, fin-and-tube heat exchangers have better heat transfer coefficients and surface area because of the addition of fins, which can be used under high temperature and high pressure conditions. Therefore, a fin-and-tube heat exchanger is selected as the evaporator in the HT cycle. By contrast, if the coolant and turbocharged air temperatures are relatively low, then using a compact, high efficiency, and low cost heat exchanger is preferable. The plate heat exchanger is used for the intercooler, the preheater, evaporator 2 and the condenser.

2.4.1. Fin-and-tube heat exchanger modeling

Table 2 Geometric dimensions of the fin-and-tube evaporator.

Items	Parameters	Units
Number of tubes in each row	9	-
Number of tube rows	20	-
Tube outer diameter	25	mm
Tube inner diameter	20	mm
Tube pitch	60	mm
Row pitch	100	mm
Fin height	12	mm
Fin width	1	mm
Rib effect coefficient	3	-
Tube row alignment	Staggered type	-
Tube material	Stainless steel 316L	-
Fin material	Stainless steel 316L	-
Inner heat transfer area	9	m^2
Tube length	8.8	m

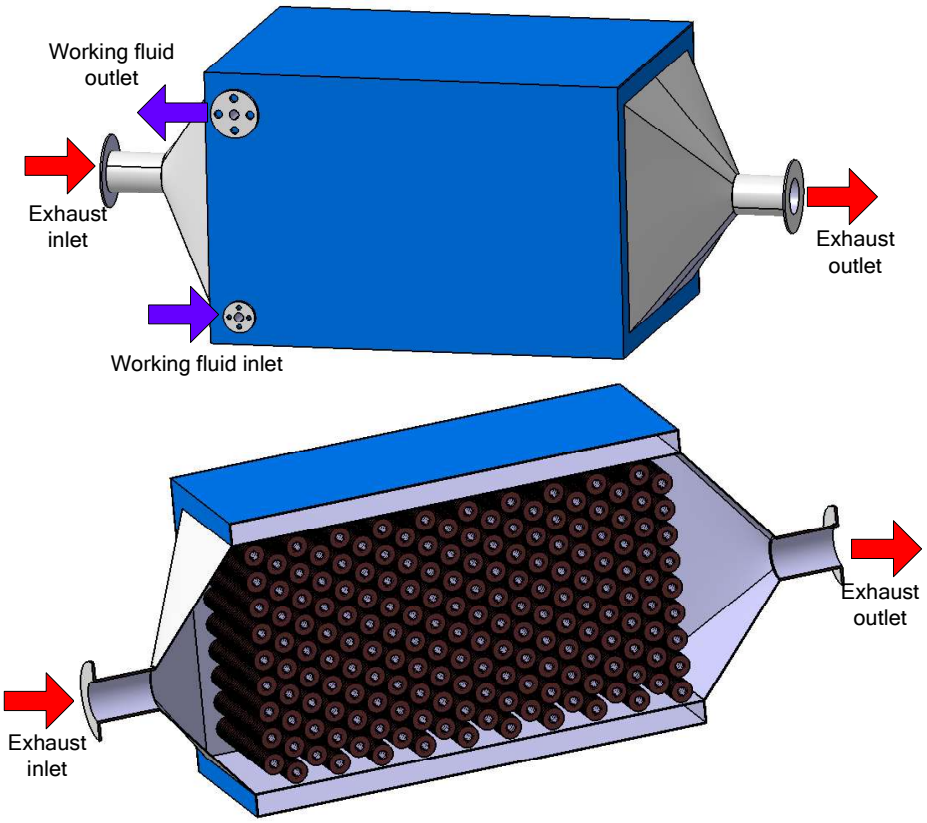

Fig. 4. Schematic of the fin-and-tube evaporator.

As shown in Fig. 2, the evaporator is divided into three zones: the preheated zone (state point H5–state point H6), the evaporation zone (state point H6–state point H7), and the superheated zone (state point H7–state point H1). The schematic and geometric dimensions of the fin-and-tube evaporator are provided in Fig. 4 and Table 2, respectively. The working fluid transfers heat inside the tube, whereas the exhaust gas transfers heat outside the tube. The overall heat transfer coefficient for each section can be expressed as:

$$\frac{1}{K_{\text{fi}}} = \frac{\beta}{h_{\text{in}}} + r_{\text{in}}\beta + \frac{\delta\beta}{\lambda} + \frac{r_{\text{out}}}{\eta} + \frac{1}{h_{\text{out}}\eta} \tag{21}$$

$$h = \frac{\lambda Nu}{d} \tag{22}$$

When the CNG engine is running under various operating conditions, the exhaust gas is always in gaseous state. The Nusselt number of the exhaust gas can be calculated using the Zhukauskas

correlation [39].

When $1000<Re<2\times10^5$,

$$Nu_{\mathrm{exh}} = 0.35\varepsilon^{0.2}\, Re_{\mathrm{exh}}^{0.6}\, Pr_{\mathrm{exh}}^{0.36}\left(\frac{Pr_{\mathrm{exh}}}{Pr_{\mathrm{exh,wall}}}\right)^{0.25} \tag{23}$$

When $Re<1000$,

$$Nu_{\mathrm{exh}} = 0.71 Re_{\mathrm{exh}}^{0.5}\, Pr_{\mathrm{exh}}^{0.36}\left(\frac{Pr_{\mathrm{exh}}}{Pr_{\mathrm{exh,wall}}}\right)^{0.25} \tag{24}$$

For the single-phase heat transfer process in the tube side, the Gnielinski correlation is used to calculate the Nusselt number [40].

$$Nu_{\mathrm{wf}} = \frac{(f/8)(Re_{\mathrm{wf}}-1000)\,Pr_{\mathrm{wf}}}{1+12.7\sqrt{f/8}\,(Pr_{\mathrm{wf}}^{2/3}-1)}\left[1+\left(\frac{d}{l}\right)^{2/3}\right]c_{\mathrm{t}} \tag{25}$$

$$f = (1.82\lg Re_{\mathrm{wf}} - 1.64)^{-2} \tag{26}$$

In the preheated zone,

$$c_{\mathrm{t}} = \left(\frac{Pr_{\mathrm{wf}}}{Pr_{\mathrm{wall}}}\right)^{0.01}, \quad \frac{Pr_{\mathrm{wf}}}{Pr_{\mathrm{wall}}} = 0.05 \sim 20 \tag{27}$$

In the superheated zone,

$$c_{\mathrm{t}} = \left(\frac{T_{\mathrm{wf}}}{T_{\mathrm{wall}}}\right)^{0.45}, \quad \frac{T_{\mathrm{wf}}}{T_{\mathrm{wall}}} = 0.5 \sim 1.5 \tag{28}$$

The working fluid is in a two-phase state in the evaporation zone, and the thermodynamic properties may vary with the vapor quality of the working fluid. Consequently, the two-phase section of the evaporator is discretized and divided into N parts. The thermodynamic properties of the working fluid in each part can be assumed as constant [32,41]. The convective heat transfer coefficient can be calculated using the Liu and Winterton correlation [42].

$$h_{\mathrm{tp,i}} = \sqrt{(F_{\mathrm{i}} h_{\mathrm{fb,i}})^2 + (S_{\mathrm{i}} h_{\mathrm{nb,i}})^2} \tag{29}$$

The forced convective heat transfer enhancement factor can be expressed as:

$$F_{\mathrm{i}}=\left[1+x_{\mathrm{i}}\,Pr_{\mathrm{l}}\left(\frac{\rho_{\mathrm{l}}}{\rho_{\mathrm{v}}}-1\right)\right]^{0.35} \tag{30}$$

The suppression factor is given by:

$$S_{\mathrm{i}}=(1+0.055F_{\mathrm{i}}^{0.1}\,Re_{\mathrm{L,i}}^{0.16})^{-1} \tag{31}$$

The Dittus–Boelter equation is used to calculate the convective heat transfer coefficient for the film boiling.

$$h_{\mathrm{fb,i}}=0.023(\lambda_{\mathrm{l}}/d)\,Re_{\mathrm{L,i}}^{0.8}\,Pr_{\mathrm{l}}^{0.4} \tag{32}$$

The convective heat transfer coefficient for the nucleate boiling can be determined using the Cooper's pool boiling correlation.

$$h_{\mathrm{nb,i}}=55p_{\mathrm{r}}^{0.12}q_{\mathrm{i}}^{2/3}(-\lg p_r)^{-0.55}M^{-0.5} \tag{33}$$

2.4.2. Plate heat exchanger modeling

The schematic and geometric dimensions of the plate heat exchanger are provided in Fig. 5 and Table 3, respectively.

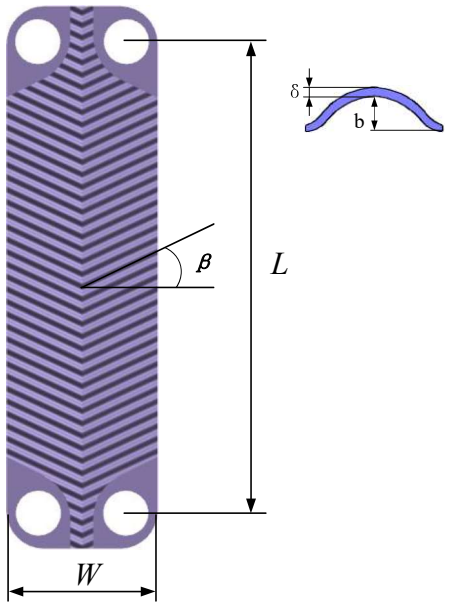

Fig. 5. Schematic of the plate heat exchanger.

Table 3 Geometric dimensions of the plate heat exchanger.

Items	Parameters	Units
Chevron angle	65	degree
Corrugation depth	3	mm
Corrugation width	4	mm
Plate thickness	0.35	mm
Plate length	0.536	m
Plate width	0.123	m

The LMTD method is also used to establish the heat transfer model of the plate heat exchanger. The overall heat transfer coefficient can be expressed as [14]:

$$\frac{1}{K_{\mathrm{pla}}}=\frac{1}{h_{\mathrm{in}}}+r_{\mathrm{in}}+\frac{\delta}{\lambda}+r_{\mathrm{out}}+\frac{1}{h_{\mathrm{out}}} \tag{34}$$

For the single-phase heat transfer process of the plate heat exchanger, the Nusselt number can be determined using the Chisholm and Wanniarachchi correlation [43].

$$Nu=0.724(\frac{6\beta}{\pi})^{0.646}Re^{0.583}Pr^{1/3} \tag{35}$$

The Reynolds number is given by:

$$Re=\frac{GD_{\mathrm{h}}}{\mu} \tag{36}$$

The mass flux can be expressed as:

$$G=\frac{m}{N\cdot W\cdot b} \tag{37}$$

The hydraulic diameter of the flow channel can be determined as:

$$D_{\mathrm{h}}=\frac{4Wb}{2(W+b)} \tag{38}$$

The two-phase heat transfer process of the plate heat exchanger is also discretized and divided into N parts. For each small part, the LMTD method is used to obtain their heat transfer coefficient. The Nusselt number for the condensation process can be calculated based on Ref. [44].

$$Nu_{\mathrm{i}}=4.118\,Re_{\mathrm{eq,i}}^{0.4}\,Pr_{\mathrm{l}}^{1/3} \tag{39}$$

The Nusselt number for the evaporation process is given based on Ref. [45].

$$Nu_{\mathrm{i}} = 1.926\, Pr_{\mathrm{l}}^{1/3}\, Bo_{\mathrm{eq,i}}^{0.3}\, Re_{\mathrm{i}}^{0.5}[1 - x_{\mathrm{i}} + x_{\mathrm{i}}(\frac{\rho_{\mathrm{l}}}{\rho_{\mathrm{v}}})^{0.5}] \tag{40}$$

The equivalent Reynolds number can be expressed as:

$$Re_{\mathrm{eq,i}} = \frac{G_{\mathrm{eq,i}} D_{\mathrm{h}}}{\mu_{\mathrm{l}}} \tag{41}$$

The equivalent boiling number can be determined as:

$$Bo_{\mathrm{eq,i}} = \frac{q''_{\mathrm{wall}}}{G_{\mathrm{eq,i}} \cdot i_{\mathrm{fg}}} \tag{42}$$

where,

$$G_{\mathrm{eq,i}} = G[1 - x_{\mathrm{i}} + x_{\mathrm{i}}(\frac{\rho_{\mathrm{l}}}{\rho_{\mathrm{v}}})^{0.5}] \tag{43}$$

3. **Engine waste heat description**

As the high temperature heat source of the dual loop ORC system, the waste heat of the CNG engine varies with the operating conditions. The distribution characteristics of the CNG engine should be determined. These characteristics are used to analyze the performance of the dual loop ORC system. In this study, a six-cylinder, in-line, turbocharged, intercooled CNG engine is adopted as the topping cycle. The main technical performance parameters of the CNG are listed in Table 4.

Table 4 The main technical performance parameters of the CNG engine.

Items	Parameters	Units
Cylinder arrangement	In-line	
Cylinder number	6	
Air intake type	Turbocharged and Intercooled	
Fuel supply	Port fuel injection	
Ignition type	Spark ignition	
Rated power	210	kW
Displacement	8.8	L
Maximum torque	1120	N.m
Stroke and cylinder bore	114×144	mm

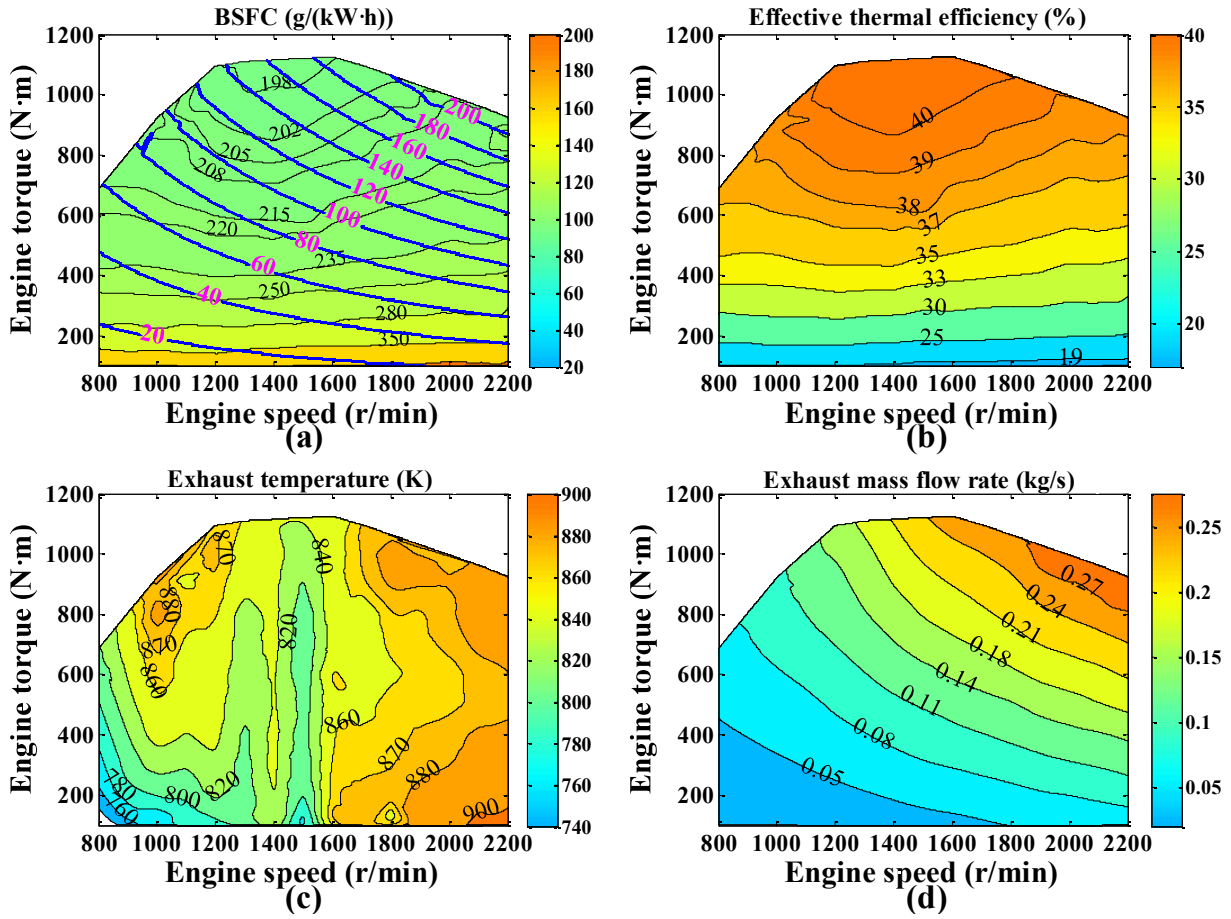

Fig. 6. Performance map of the CNG engine.

Fig. 6(a) shows the variation of the power output and BSFC (brake specific fuel consumption) of the CNG engine under various operating conditions. The blue contour line indicates the power output of the CNG engine. At the rated condition, the power output of the CNG engine reaches a maximum value of 210 kW. Fig. 6(b) shows the effective thermal efficiency of the CNG engine under various operating conditions. The effective thermal efficiency is mainly influenced by the engine torque. For the medium-high load regions of the CNG engine, the effective thermal efficiency is above 35%. Fig. 6(c) shows the variation of the exhaust temperature with the engine operating conditions. The exhaust temperature is over 800 K under most of the operating conditions. At the low speed and low torque regions of the CNG engine, the exhaust temperature increases with

engine speed and torque. By contrast, the variation of the exhaust temperature is more complicated at medium-high speed and medium-high load regions. Fig. 6(d) shows the variation of the exhaust mass flow rate under various operating conditions, which is mainly influenced by intake air and fuel consumption. Under the rated condition, the exhaust mass flow rate achieves a maximum value of 0.31 kg/s.

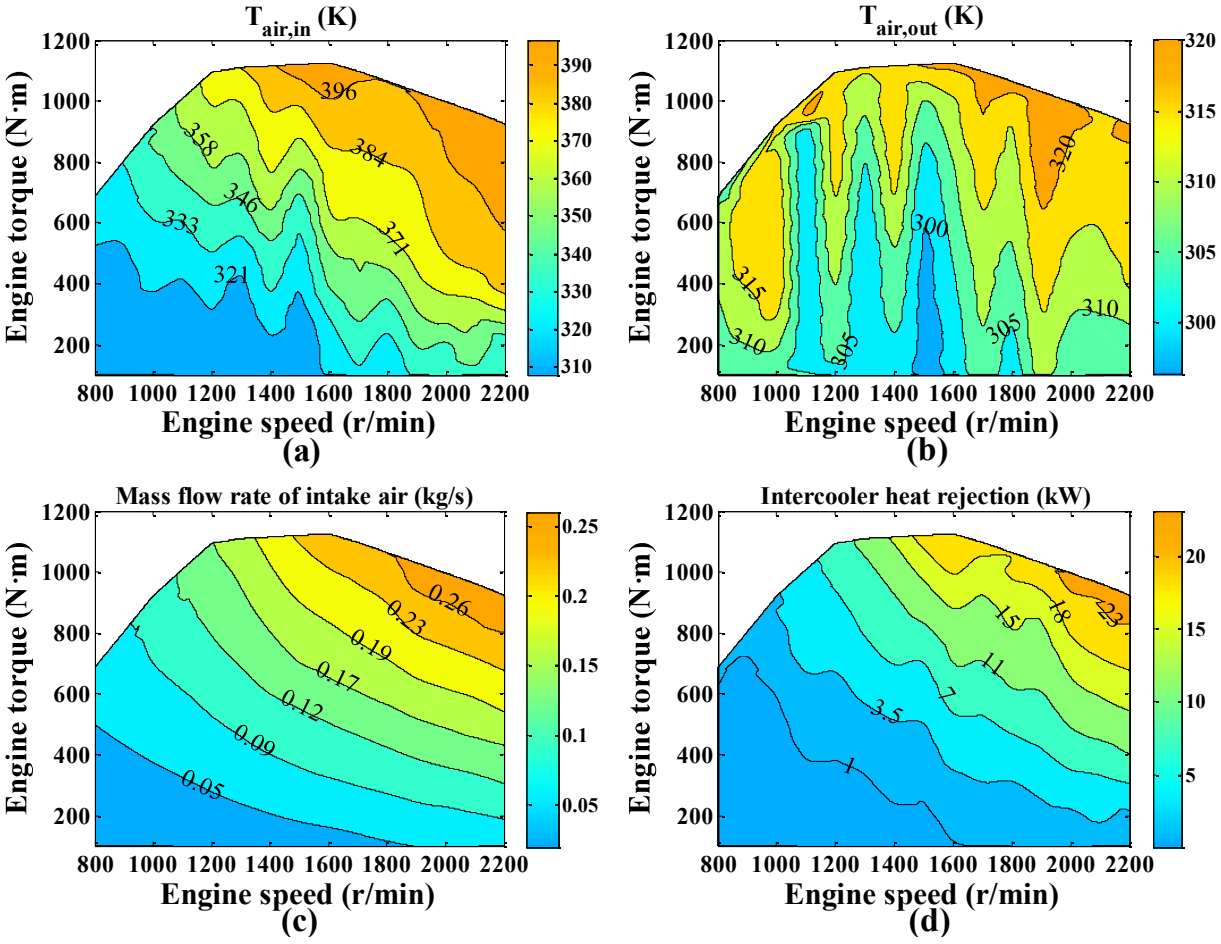

Fig. 7. Waste heat characteristics of intercooler.

For IC engines equipped with a turbocharger, intake air temperature can increase significantly after the compression process. Fig. 7(a) shows the variation in intake air temperature at the inlet of the intercooler under various operating conditions. The intake air temperature at the inlet of the intercooler is within the range of 308–410 K over the whole operating range of the CNG engine. Fig.

7(b) shows the variation in the turbocharged air temperature at the outlet of the intercooler. The variation of the turbocharged air temperature at the outlet of the intercooler is complicated. As shown in Fig. 7(b), the turbocharged air temperature at the outlet of the intercooler is within a small range of 298–323 K. Fig. 7(c) shows the variation in the intake air mass flow rate under various operating conditions. The intake air mass flow rate increases with engine speed and torque. The intake air mass flow rate is within the range of 0.02–0.29 kg/s over the whole operating range of the CNG engine. Fig. 7(d) shows the variation in the rejected heat from the intercooler with the engine operating conditions. Similar to the intake air mass flow rate, the rejected heat from the intercooler also increases with engine speed and torque. When the CNG engine is operating at the medium-high speed and medium-high load regions, the rejected heat from the intercooler is within the range of 10–26 kW. The rejected heat from the intercooler can be used to preheat the subcooled working fluid at the outlet of the pump given the configuration characteristics of the dual loop ORC system.

Fig. 8(a) shows the variation in the coolant temperature at the inlet of the CNG engine. The coolant temperature at the inlet of the CNG engine is within the range of 350–360 K. Fig. 8(b) shows the variation in the coolant temperature at the outlet of CNG engine. Similar to the coolant temperature at the inlet of the CNG engine, the coolant temperature at the outlet of the CNG engine varies within a small range. The coolant temperature at the outlet of CNG engine is kept nearly constant at 360 K over the whole operating range of the CNG engine,. Fig. 8(c) shows the variation in the coolant mass flow rate with the engine operating conditions. The coolant mass flow rate is mainly influenced by engine speed, that is, the coolant mass flow rate increases gradually with engine speed. The coolant mass flow rate is within the range of 1.55–3.37 kg/s under various operating

conditions of the CNG engine. Fig. 8(d) shows the variation in the waste heat of the coolant over the whole operating range. The waste heat of the coolant increases with engine speed and torque in the medium-high load regions. In the low load regions, the waste heat of the coolant is mainly affected by engine speed. The waste heat of the coolant is within the range of 28–88 kW over the whole operating range of the CNG engine. Compared with Fig. 7, the waste heat of the coolant is evidently higher in quantity than that of the rejected heat from the intercooler because of its higher mass flow rate and specific heat capacity. The temperature difference of the coolant between the inlet and outlet of the CNG engine is relatively small, and thus, the engine coolant can be used to heat the working fluid during the evaporation process in the LT cycle to reduce irreversible loss.

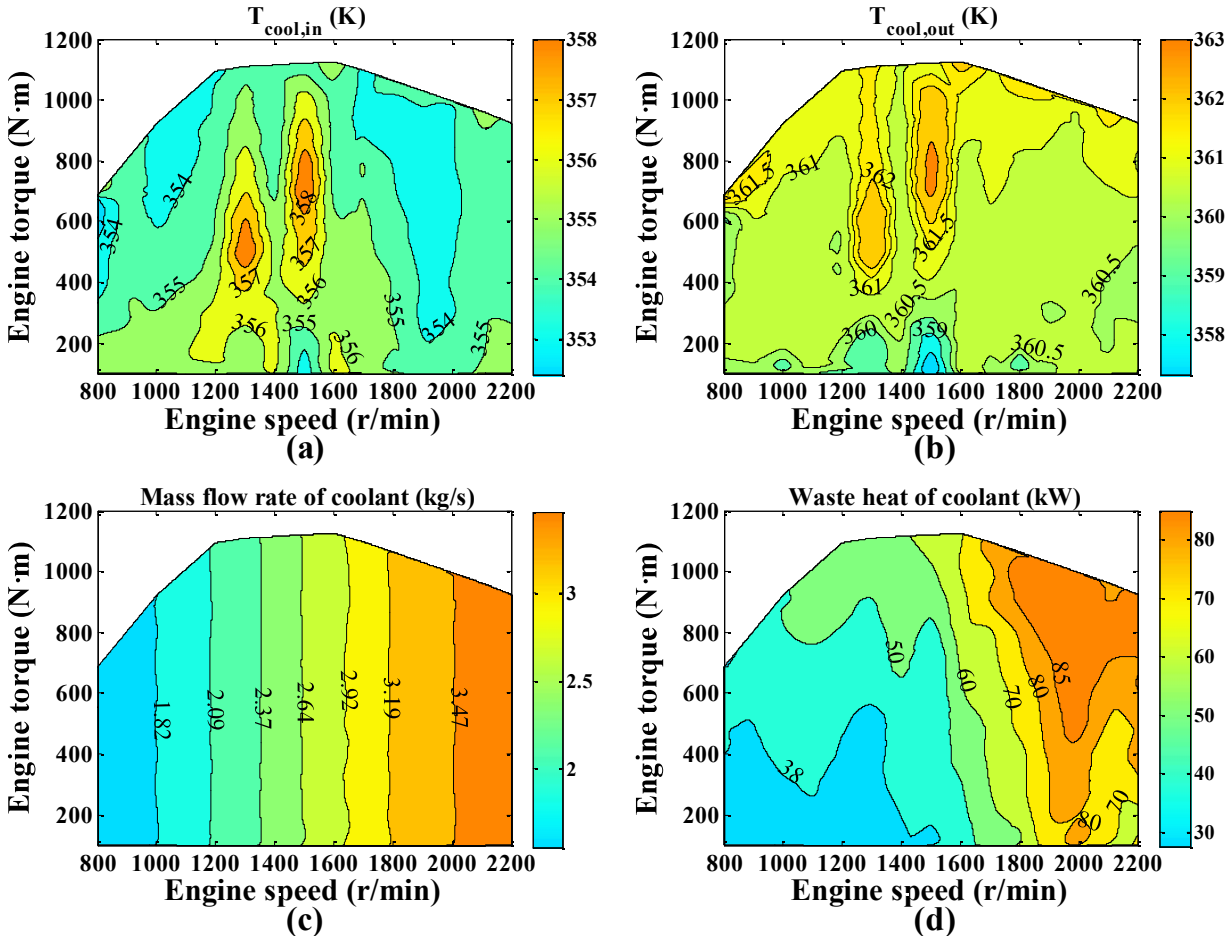

Fig. 8. Waste heat characteristics of coolant.

4. **Multi-objective optimization**

4.1. Optimization modeling

The aforementioned analysis indicates that the waste heat from the IC engine mainly depends on its operating conditions. The distribution characteristics of waste heat vary with operating conditions. The ORC system generally involves multiple parameters. The more complex the system configurations are, the more the parameters are involved. As shown in Figs. 2 and 3, the dual loop ORC system involves more operating parameters compared with the simple ORC system. In the HT cycle, the operating parameters mainly include evaporation pressure, superheat degree and condensation temperature. In the LT cycle, the operating parameters are evaporation and condensation temperatures. Furthermore, the exhaust temperature at the outlet of evaporator 1 affects the heat transfer rate. From the basic principles of the steam power cycle, increasing evaporation pressure, superheating the steam to high temperatures, and decreasing condensation temperature will increase power output and thermal efficiency. By contrast, the thermodynamic performance is improved at the expense of the economic indicators, particularly for the heat transfer area. Therefore, optimizing the synergy variation law between the dual loop ORC system and the IC engine is difficult when only the theoretical analysis method is used. In addition, this study involves coordinated optimization between thermodynamic performance and heat transfer characteristics. Adopting the multi-objective and multi-parameter method to establish the optimization model is preferable.

In recent years, the genetic algorithm has been widely applied to solve multi-objective optimization problems of the thermodynamic system [5,14,26–28,32,41]. The GA is an optimization method

based on natural selection and biological evolutionary theory. It adopts three main types of operators at each step to create the next generation from the current population. The optimization method typically starts from a population of randomly generated individuals, proceeds as an iterative process. In each generation, the fitness function of each individual is evaluated. Fit individuals are randomly selected from the current population to be parents and used to produce a new generation. The algorithm generally terminates when either a maximum number of generations has been reached, or a satisfactory fitness level has been achieved [46].

In this study, the GA is used to conduct multi-objective optimization of the dual loop ORC system. The net power output and the total heat transfer area are selected as the objective functions. Meanwhile, the decision variables are the evaporation pressure, superheat degree and condensation temperature of the HT cycle, along with the evaporation and condensation temperatures of the LT cycle, and the exhaust temperature at the outlet of evaporator 1. For multi-objective optimization problems, the output results depend on selecting the input parameters. This study also explains how thermodynamic parameters affect the dual loop ORC system by considering thermodynamic performance and heat transfer characteristics under various operating conditions of a CNG engine. Therefore, only six of the key thermodynamic parameters are considered in this study. The effect of different input parameters on the output results of the dual loop ORC system will be part of the future work of the authors. The multi-objective optimization model for the dual loop ORC system can be expressed as:

$$\max(\dot{W}_{\text{net}}) = f(P_{\text{H7}}, T_{\text{H1}}, T_{\text{H4}}, T_{\text{L1}}, T_{\text{L4}}, T_{\text{exh,out}}) \tag{44}$$

$$\min(A_{\text{tot}}) = f(P_{\text{H7}}, T_{\text{H1}}, T_{\text{H4}}, T_{\text{L1}}, T_{\text{L4}}, T_{\text{exh,out}}) \tag{45}$$

The logical bounds of the decision variables depend on the practical operating conditions of the dual loop ORC system. The logical bounds of the decision variables are listed in Table 5. The flowchart of the optimization procedure is shown in Fig. 9.

Table 5 Lower and upper bounds of decision variables.

Decision variables	Lower bound	Upper bound
P_{H7} (MPa)	1	3
T_{H1} (K)	0	20
T_{H4} (K)	350.15	360.15
T_{L1} (K)	323.15	343.15
T_{L4} (K)	298.15	318.15
$T_{exh,out}$ (K)	393.15	423.15

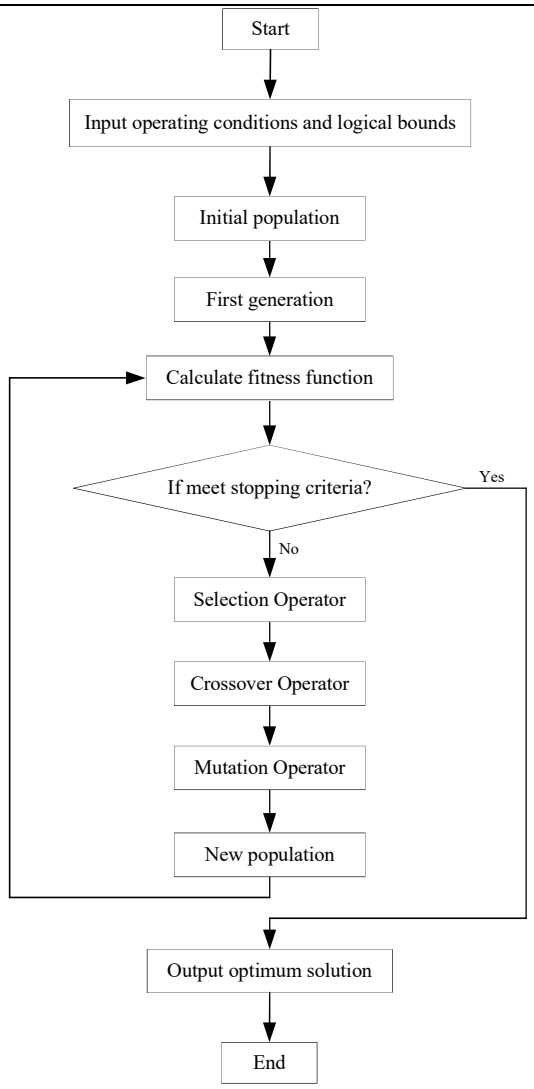

Fig. 9. Flow chart of the optimization procedure.

4.2. Pareto optimization methodology

The Pareto optimization methodology is generally used to solve multiple criteria decision making problems. This methodology provides new insights into optimization problems with multiple conflicting objectives [47]. Unlike single-objective optimization problems, multi-objective optimization involves multiple objective functions that should be optimized simultaneously. Objective functions typically conflict with one another, and thus, no single optimal solution that simultaneously optimizes each objective is available [48]. Accordingly, multi-objective optimization using an evolutionary algorithm normally generates a set of optimal solutions, which is called a Pareto optimal set. Each solution in a Pareto optimal set is regarded as a Pareto optimal solution. A feasible solution for a multi-objective optimization problem is referred to as a Pareto optimal solution if no other feasible solution that will lead to an improvement in one objective without deteriorating in at least one other objective is available [47]. Meanwhile, a trade-off between these objective functions should be considered. The investigator can select the ultimate solution among the Pareto optimal sets based on the practical requirements. The decision-making process is generally used to identify and select the final optimal solution based on the values and preferences of the decision-maker.

4.3. Evaluation of the GA

The Pareto frontier is related to the parameter setting of the optimization model, and thus, affect the Pareto solutions. Consequently, the optimization model is first verified before solving the optimization problems. For the GA optimization model, the related parameters include population size, tournament size, and crossover fraction. Using the CNG engine rated condition as an example,

the Pareto frontier should be well-distributed within a small region [27]. Fig. 10 shows the variation in the Pareto frontier with population size. When population size is 100, 200, and 300, the Pareto frontier is well-distributed. When population size increases from 100 to 300, the Pareto frontier gradually converges within a small region. Furthermore, when population size is 400, the Pareto frontier exhibits a mutation. Fig. 11 shows the variation in the Pareto frontier with tournament size. A well-distributed Pareto frontier can be achieved only when tournament size is 6. Fig. 12 shows the variation in the Pareto frontier as crossover fraction increases from 0.2 to 0.8. The Pareto frontier has an ideal distribution only when the crossover fraction is 0.8. On the basis of the aforementioned verification results, the parameter settings of the optimization model are listed in Table 6.

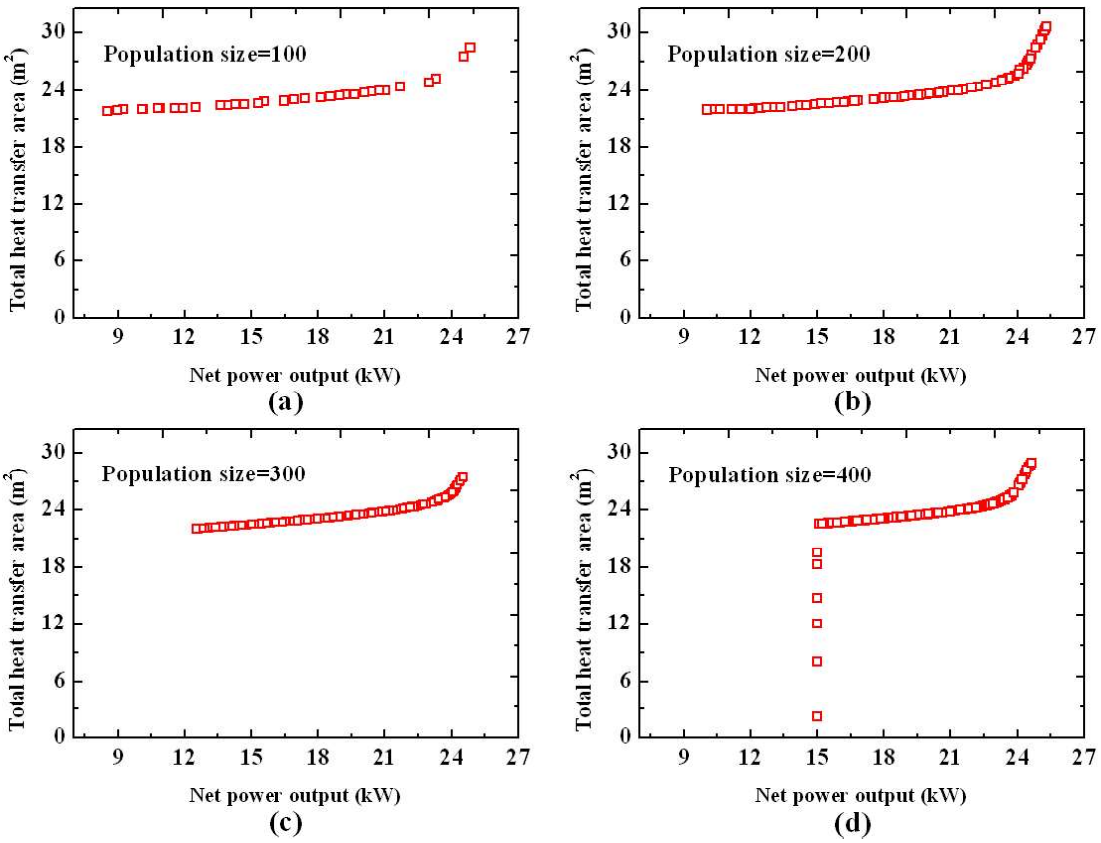

Fig. 10. Pareto frontier under different population size.

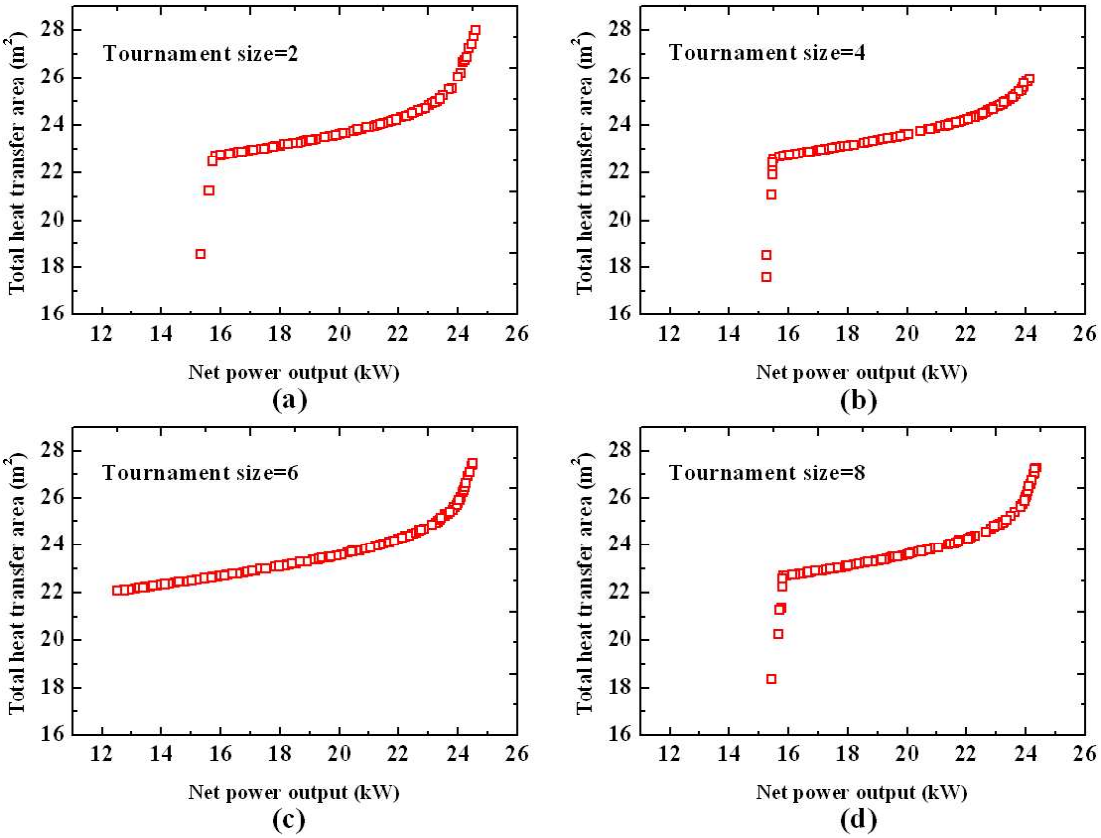

Fig. 11. Pareto frontier under different tournament size.

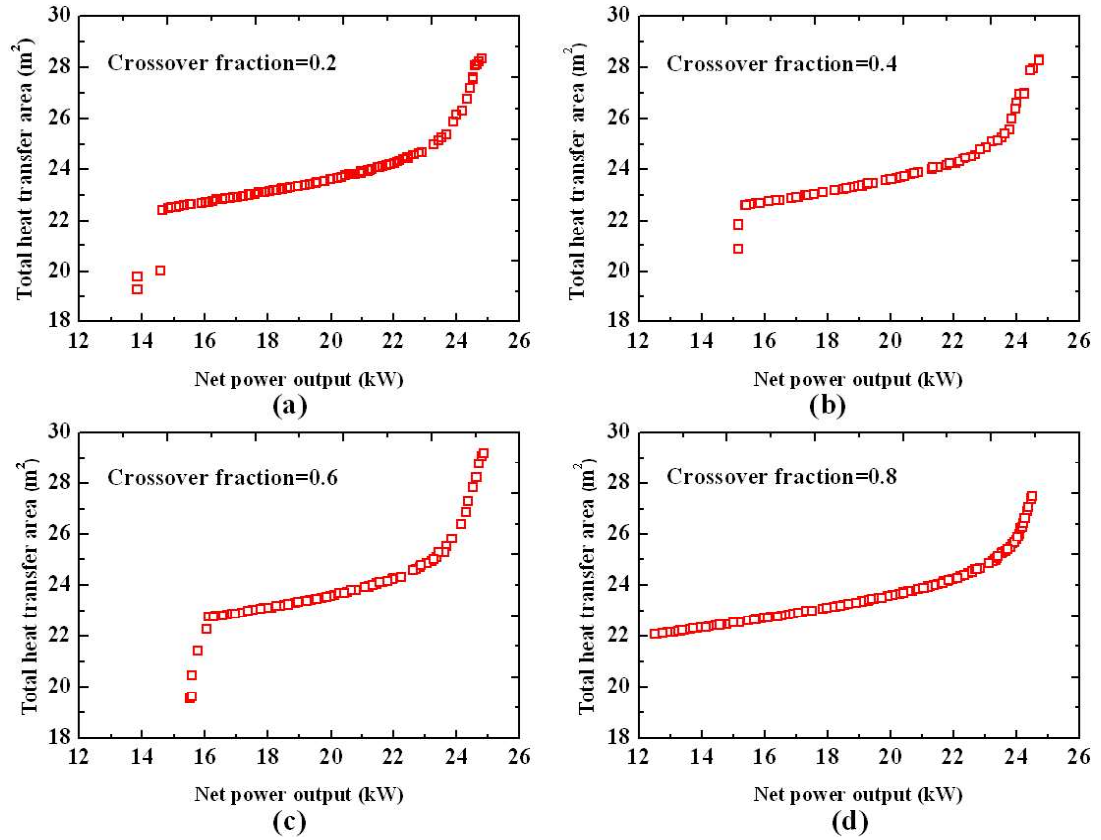

Fig. 12. Pareto frontier under different crossover fraction.

Table 6 Parameters setting of genetic algorithm.

Parameters	Value
Population size	300
Selection function	Tournament
Tournament size	6
Crossover fraction	0.8
Mutation function	Adaptive feasible
Crossover function	Scattered
Stop generations	1200

4.4. Decision-making for multi-objective optimization

In a multi-objective optimization problem, every objective may interact with and even contradict one another. Therefore, the selection of optimal solutions in the decision making process is complicated. TOPSIS (Technique for Order Preference by Similarity to an Ideal Solution) is an effective method in multi-objective decision making problems [49–51]. The basic principle of the TOPSIS method is to choose the alternatives with the shortest geometric distance from the positive ideal solution and the longest geometric distance from the negative ideal solution. The objective vectors should be non-dimensionalized before the multi-objective decision making process given that the dimension of each optimization objective may be different [49]. In the present study, the TOPSIS method is used in the decision making process after Euclidian non-dimensionalization.

In the TOPSIS method, the spatial distance of each solution on the Pareto frontier from the ideal point is defined as:

$$d_{i+} = \sqrt{\sum_{j=1}^{n} (F_{ij} - F_j^{ideal})^2} \tag{46}$$

where F_j^{ideal} is the ideal solution for *j*th objective obtained from a single-objective optimization.

The spatial distance of each solution on the Pareto frontier from the non-ideal point is defined as:

$$d_{i-} = \sqrt{\sum_{j=1}^{n} (F_{ij} - F_j^{non\text{-}ideal})^2} \quad (47)$$

where $F_j^{non\text{-}ideal}$ is the non-ideal solution for jth objective obtained from a single-objective optimization.

The closeness coefficient is defined as:

$$C_i = \frac{d_{i-}}{d_{i+} + d_{i-}} \quad (48)$$

In the TOPSIS decision-making method, a solution with the maximum C_i is selected as the final solution. Using the CNG engine rated condition as an example, the detailed decision making process is illustrated in Fig. 13.

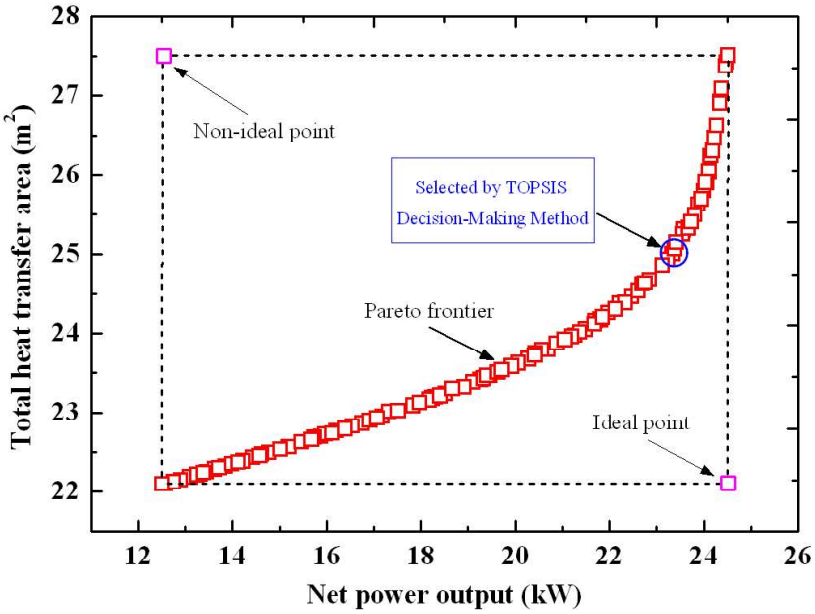

Fig. 13. Pareto frontier for multi-objective optimization.

5. Results and discussion

The performance of the dual loop ORC system is optimized using the GA based on the established thermodynamic, heat transfer, and optimization models. The sensitivity analysis should be considered for an optimization process. First, the effects of six different operating parameters on the objective functions are investigated. During this process, the value of the selected parameter varies

according to its logical bounds (as shown in Table 5), whereas the other parameters are set equal to the median value of the logical bounds. Using the engine rated condition as an example, Figs. 14 and 15 illustrate the effects of the six different operating parameters on the net power output and total heat transfer area.

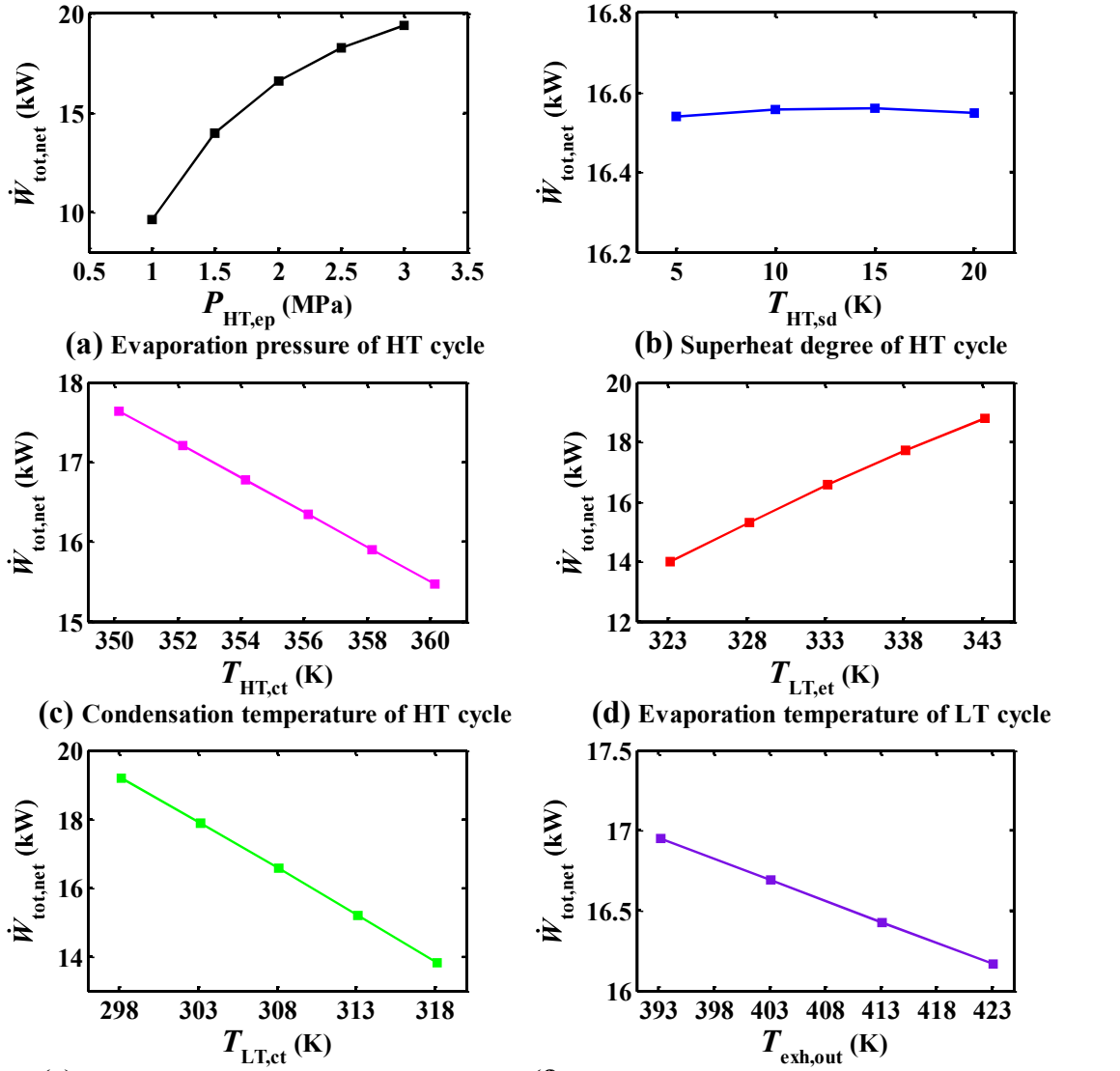

(a) Evaporation pressure of HT cycle **(b)** Superheat degree of HT cycle

(c) Condensation temperature of HT cycle **(d)** Evaporation temperature of LT cycle

(e) Condensation temperature of LT cycle **(f)** Exhaust temperature at the outlet of evaporator 1

Fig. 14. Effects of the operating parameters on the net power output.

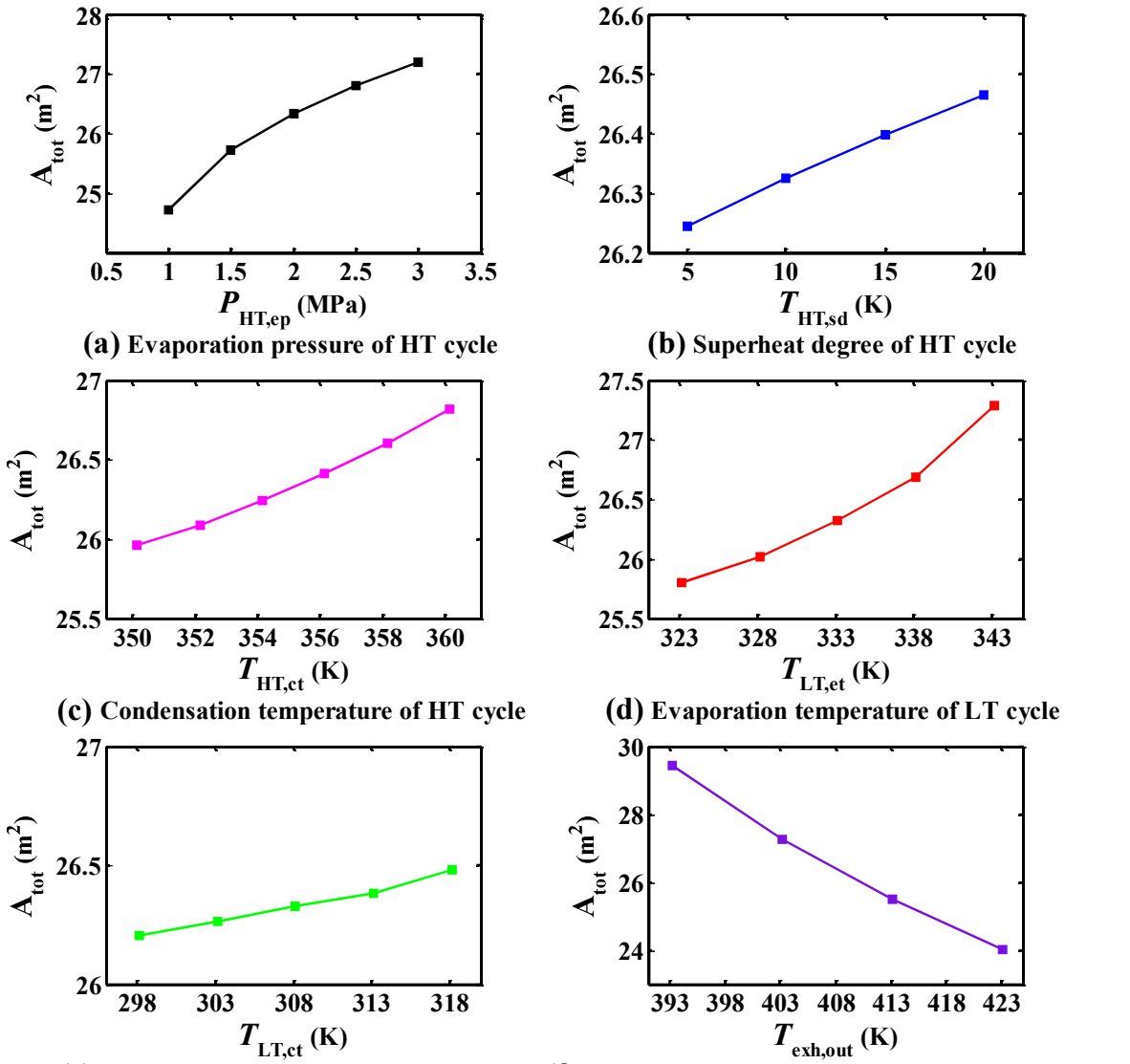

Fig. 15. Effects of the operating parameters on the total heat transfer area.

5.1. Sensitivity analysis

5.1.1. Effect of the evaporation pressure of the HT cycle

The variations in the net power output ($\dot{W}_{tot,net}$) and the total heat transfer area (A_{tot}) with the evaporation pressure of the HT cycle ($P_{HT,ep}$) are shown in Figs. 14(a) and 15(a), respectively. Notably, $\dot{W}_{tot,net}$ and A_{tot} increase significantly with $P_{HT,ep}$. When $P_{HT,ep}$ varies from 1 MPa to 3 MPa, $\dot{W}_{tot,net}$ increases from 9.66 kW to its maximum value of 19.36 kW. This increase mainly

occurs as a result of an increase in the enthalpy difference between the inlet and outlet of expander 1. Meanwhile, A_{tot} increases from 24.72 m^2 to 27.21 m^2 with increasing $P_{HT,ep}$. When $P_{HT,ep}$ increases, the enthalpy difference between the inlet and outlet of evaporator 1 also increases, thereby increasing the heat transfer rate of evaporator 1. Therefore, increasing $P_{HT,ep}$ results in an increase in A_{eva1}.

5.1.2. Effect of the superheat degree of the HT cycle

Figs. 14(b) and 15(b) show the effect of the superheat degree of the HT cycle ($T_{HT,sd}$) on two objective functions. As shown in Fig. 14(b), $T_{HT,sd}$ has nearly no effect on the net power output because an increment in $T_{HT,sd}$ leads to a small change in enthalpy at state point H1 presented in Fig. 2. The results presented in Fig. 15(b) indicate that A_{tot} increases from 26.24 m^2 to 26.46 m^2 with increasing $T_{HT,sd}$. The appearance of a superheat zone yields an increase in A_{tot}. However, the heat transfer rate in a superheat zone is small.

5.1.3. Effect of the condensation temperature of the HT cycle

Figs. 14(c) and 15(c) show the variations of the net power output and the total heat transfer area with the condensation temperature of the HT cycle ($T_{HT,ct}$), respectively. $\dot{W}_{tot,net}$ decreases dramatically with the increase in $T_{HT,ct}$, whereas A_{tot} exhibits the opposite trend. When $T_{HT,ct}$ varies from 350 K to 360 K, $\dot{W}_{tot,net}$ decreases from 17.64 kW to 15.47 kW. The increment in $T_{HT,ct}$ leads to a reduction in the enthalpy difference between the inlet and outlet of expander 1, which in turn, decreases the net power output of the HT cycle. Simultaneously, increasing $P_{HT,ep}$ increases the heat transfer rate of the preheater. Hence, the heat transfer area of the preheater increases accordingly.

5.1.4. Effect of the evaporation temperature of the LT cycle

The effect of the evaporation temperature of the LT cycle $T_{\mathrm{LT,et}}$ on the net power output and the total heat transfer area is shown in Figs. 14(d) and 15(d), respectively. Similar to the effect of $P_{\mathrm{HT,ep}}$, $\dot{W}_{\mathrm{tot,net}}$ and $\mathrm{A_{tot}}$ increase with increasing $T_{\mathrm{LT,et}}$. By contrast, the increase in $T_{\mathrm{LT,et}}$ widens the enthalpy difference between the inlet and the outlet of expander 2, which increases the net power output of the HT cycle. When $T_{\mathrm{LT,et}}$ varies from 323 K to 343 K, the $\dot{W}_{\mathrm{tot,net}}$ increases from 13.98 kW to 18.79 kW. On the contrary, increasing $T_{\mathrm{LT,et}}$ leads to an increase in the heat transfer areas of the preheater and evaporator 2.

5.1.5. Effect of the condensation temperature of the LT cycle

Figs. 14(e) and 15(e) show the variations in the net power output and the total heat transfer area with the condensation temperature of the LT cycle ($T_{\mathrm{LT,ct}}$), respectively. As shown in Fig. 14(e), $\dot{W}_{\mathrm{tot,net}}$ decreases significantly with increasing $T_{\mathrm{LT,ct}}$. A high condensation temperature of the vapor power cycles generally leads to a decrease in the power output. $\mathrm{A_{tot}}$ exhibits a small increment with the increase in $T_{\mathrm{LT,ct}}$. When $T_{\mathrm{LT,ct}}$ varies from 298 K to 318 K, $\mathrm{A_{tot}}$ increases from 26.21 $\mathrm{m^2}$ to 26.48 $\mathrm{m^2}$.

5.1.6. Effect of the exhaust temperature at the outlet of evaporator 1

Figs. 14(f) and 15(f) show the variations in the net power output and the total heat transfer area with the exhaust temperature at the outlet of evaporator 1 ($T_{\mathrm{exh,out}}$), respectively. Both objective functions decrease significantly with the increase in $T_{\mathrm{exh,out}}$. When $T_{\mathrm{exh,out}}$ increases, the heat transfer rate in evaporator 1 decreases dramatically decreases, thereby decreasing the mass flow rate of the HT cycle. Meanwhile, the decrease of the heat transfer rate in evaporator 1 and the mass flow rate of the HT cycle lead to a decrease in $\dot{W}_{\mathrm{tot,net}}$ and $\mathrm{A_{tot}}$.

5.2. Parametric optimization and thermodynamic analysis of the dual loop ORC system

Fig. 16 shows the optimization results of the operating parameters of the dual loop ORC system under various conditions of the CNG engine. The optimal evaporation pressure of the HT cycle is illustrated in Fig. 16(a). The optimal evaporation pressure of the HT cycle is higher than 2.2 MPa over the whole operating range of the CNG engine. The optimal evaporation pressure of the HT cycle is in the range of 2.5–2.9 MPa under most operating conditions. When the dual loop ORC system is used for the cascade utilization of the IC engine, the evaporation pressure of the HT cycle should be as high as possible to allow a reasonable temperature gradient for the LT cycle. In addition, the variation in the evaporation pressure of the HT cycle is less than 1 MPa, which is beneficial for the practical control of the dual loop ORC system. Fig. 16(b) shows the optimal superheat degree of the HT cycle under various operating conditions of the CNG engine. The optimal superheat degree is less than 10 K under most operating conditions. The optimal superheat degree is higher than 10 K only for a few high speed and high load operating points. That is, a high superheat degree of the HT cycle does not result in an improved performance of the dual loop ORC system. The optimal superheat degree of the HT cycle is in the range of 0.43–12.35 K over the whole operating range of the CNG engine. Fig. 16(c) shows the optimal condensation temperature of the HT cycle under various operating conditions. The optimal condensation temperature is kept nearly constant at 350.15 K. The variation in the operating conditions of the CNG engine has also been demonstrated to slightly influence the optimal condensation temperature of the HT cycle. By contrast, the optimal condensation temperature of the HT cycle is close to its lower bound. A low condensation temperature will ensure a large enthalpy difference between the inlet and the outlet of the expander. Fig. 16(d) shows the optimal evaporation temperature of the LT cycle under various

operating conditions. The optimal evaporation temperature of the LT cycle is within the range of 339–343 K over the whole operating range of the CNG engine, and increases with a decreasing engine torque. A comparison between Fig. 16(d) and Table 5 indicates that the optimal evaporation temperature of the LT cycle is close to its upper bound. Fig. 16(e) shows the optimal condensation temperature of the LT cycle under various operating conditions of the CNG engine. The optimal condensation temperature of the LT cycle is kept nearly constant at 298.15 K. This value is close to its lower bound. Similar to the HT cycle, the lower condensation temperature is beneficial for the thermodynamic performance of the ORC system. Fig. 16(f) shows the optimal exhaust temperature at the outlet of evaporator 1 under various operating conditions. The optimal exhaust temperature at the outlet of the evaporator 1 is kept nearly constant at 423.15 K under most operating conditions. The optimal exhaust temperature at the outlet of evaporator 1 is close to 422.15 K only at a few low speed and low load operating points. A comparison between Fig. 16(f) and Table 5 indicates that the optimal exhaust temperature at the outlet of evaporator 1 is close to its upper bound. The heat transfer rate increases with decreasing exhaust temperature at the outlet of evaporator 1, which will result in an increase in the mass flow rate of the working fluid and the power output. By contrast, the high exhaust temperature at the outlet of evaporator 1 also causes an increase in the heat transfer area and in investment cost.

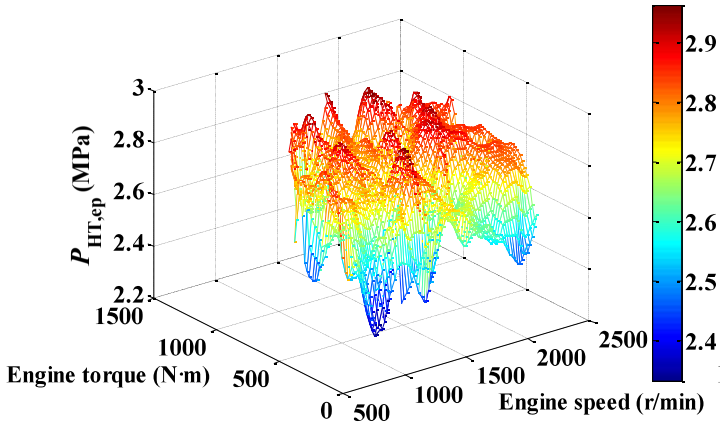

(a) Optimal evaporation pressure of HT cycle

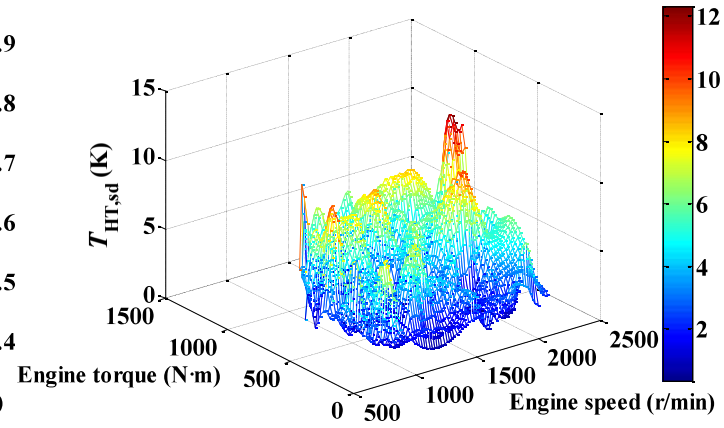

(b) Optimal superheat degree of HT cycle

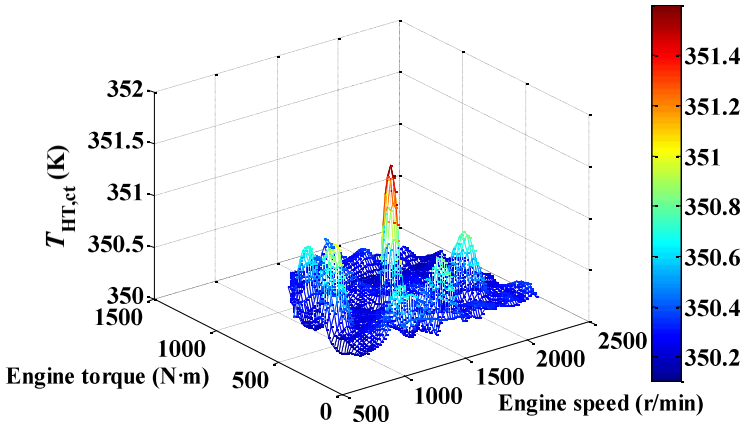

(c) Optimal condensation temperature of HT cycle

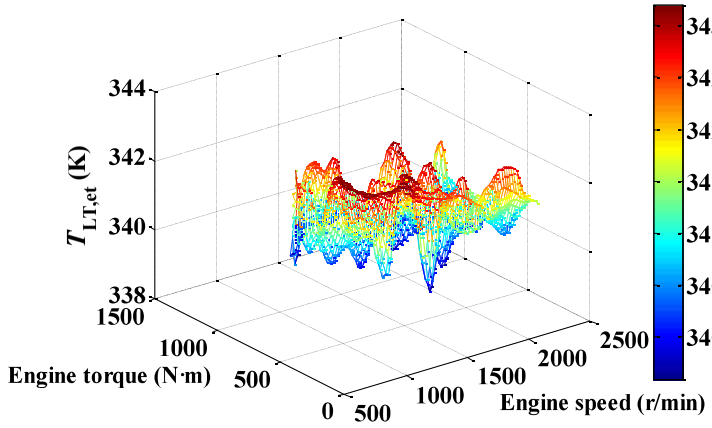

(d) Optimal evaporation temperature of LT cycle

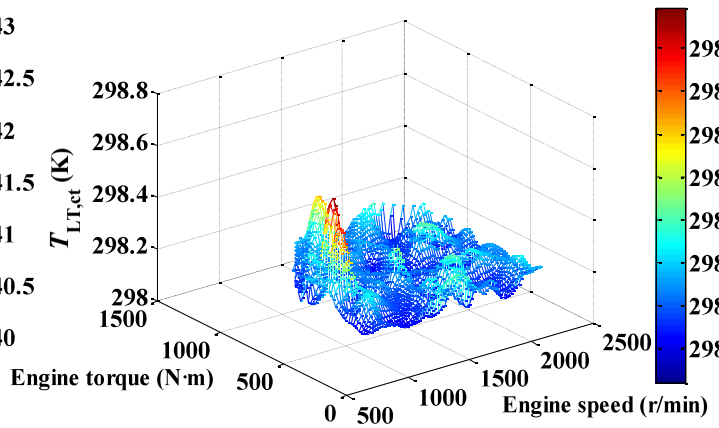

(e) Optimal condensation temperature of LT cycle

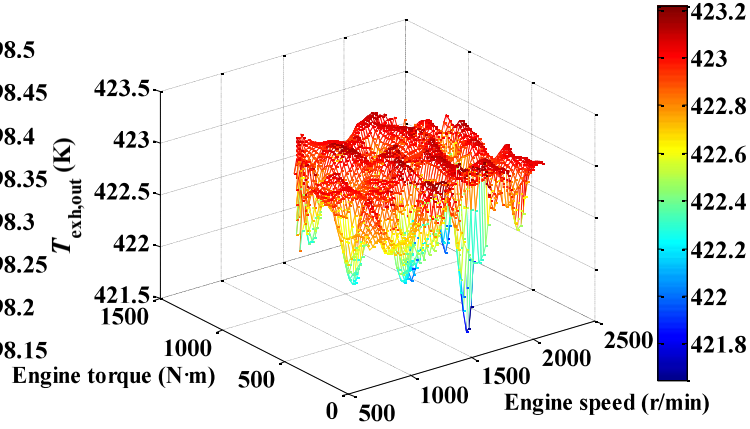

(f) Optimal exhaust temperature

Fig. 16. Optimization results of the operating parameters of the dual loop ORC system.

Fig. 17 shows the optimization results of the thermodynamic indicators of the dual loop ORC system, including the net power output and thermal efficiency under various operating conditions of the CNG engine. The optimization results of the net power output of the dual loop ORC system is presented in Fig. 17(a). The net power output of the dual loop ORC system is mainly influenced by the operating conditions of the CNG engine, and increases with engine speed and engine torque. When these results are combined with those shown in Figs. 6–8, a conclusion can be drawn that the waste heat generated from the CNG engine increases with engine speed and engine torque, which will result in an increase in the heat transfer rate, the mass flow rate of the working fluid, and the net power output. The net power output of the dual loop ORC system is within the range of 1.84–23.62 kW over the whole operating range of the CNG engine. Under the rated condition, the net power output of the dual loop ORC system achieves a maximum value of 23.62 kW. Fig. 17(b) shows the optimization result of the thermal efficiency of the dual loop ORC system. The engine torque significantly influences the thermal efficiency of the dual loop ORC system. Moreover, the thermal efficiency of the dual loop ORC system increases slightly with increasing engine torque. The thermal efficiency of the dual loop ORC system is in the range of 8.79%–10.17%. When the CNG engine operates under medium-high speed and medium-high load regions, the thermal efficiency of the dual loop ORC system is within the range of 9.5%–10%. As indicated in the aforementioned analysis, the dual loop ORC system is an effective method for recovering the waste heat of IC engines, particularly in the medium-high speed and medium-load regions.

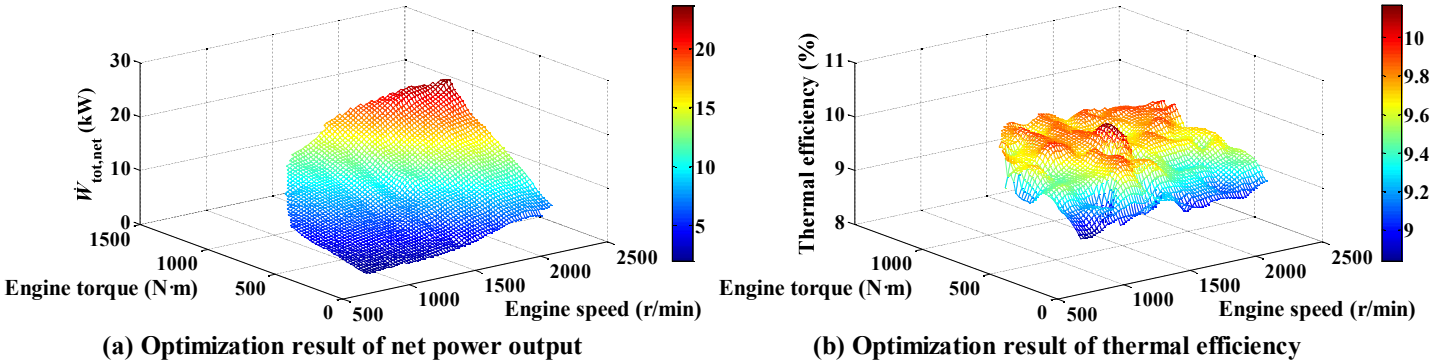

(a) Optimization result of net power output (b) Optimization result of thermal efficiency

Fig. 17. Optimization results of the net power output and thermal efficiency of the dual loop ORC system.

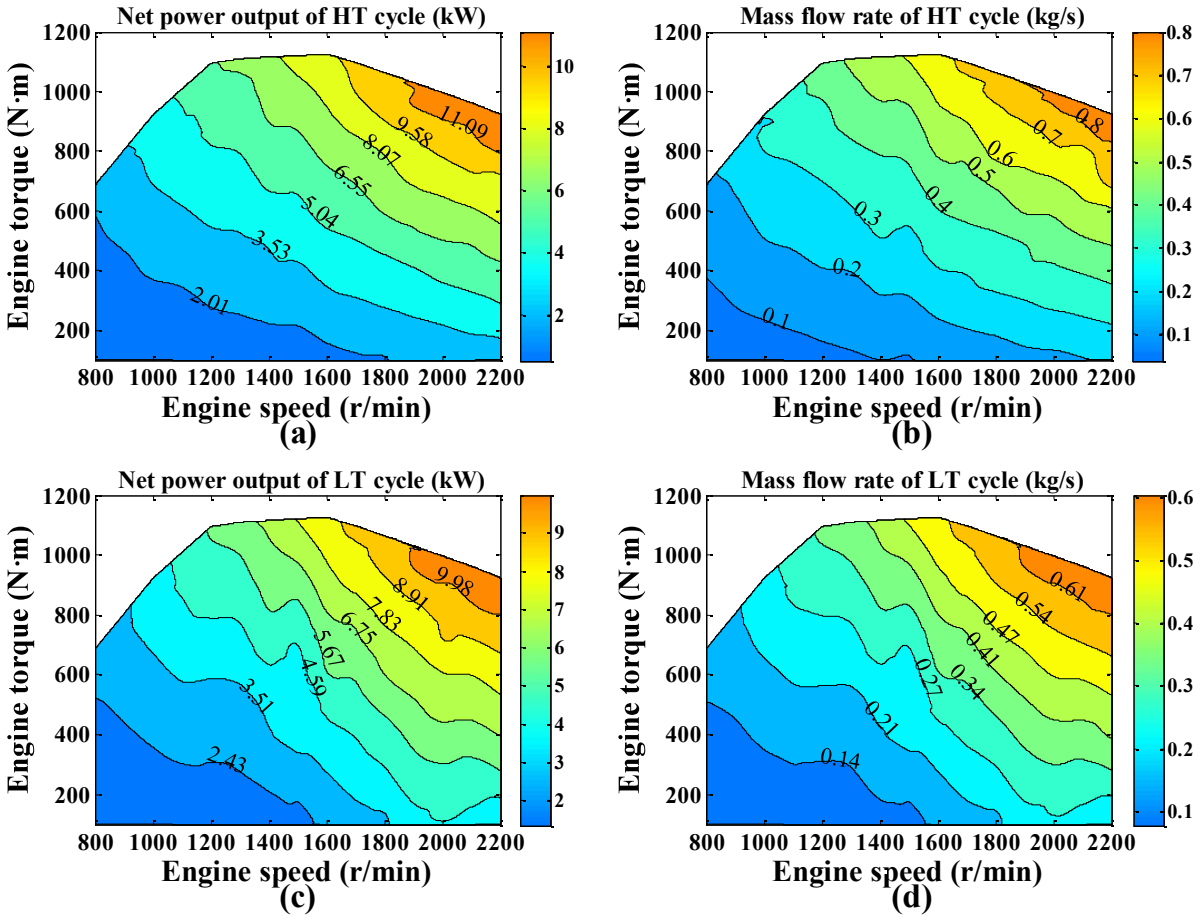

Fig. 18. Variation of the net power output and mass flow rate for HT and LT cycles.

Fig. 18 shows the net power output and the mass flow rate of the working fluid for the HT and LT cycles under various operating conditions of the CNG engine. The net power output and the mass flow rate of the working fluid for both cycles increase with engine speed and torque. As shown in

Figs. 18(a) and (c), the net power output of the HT cycle is higher than that of the LT cycle under medium-high speed and medium-high load regions. The net power output of the HT cycle is within the range of 0.49–12.56 kW, whereas that of the LT cycle is within the range of 1.35–11.06 kW. Figs. 18(b) and (d) show the variation in the mass flow rate of the working fluid under various operating conditions. Similar to the net power output, the mass flow rate of the working fluid for the HT cycle is higher than that for the LT cycle, which mainly depends on the heat transfer rate for both cycles. The mass flow rate of the working fluid for the HT cycle is within the range of 0.04–0.87 kg/s, whereas that of the LT cycle is within the range of 0.08–0.67 kg/s.

Fig. 19 shows the power consumptions of the pumps under various operating conditions of the CNG engine. Note that the back work ratio ($r_{\mathrm{bw}} = \dot{W}_{\mathrm{p}} / \dot{W}_{\mathrm{exp}}$) of the large-scale power cycle is very small and can be neglected. However, the pump efficiency in small-scale ORC system is usually below 30%, and thus the power consumption of the pump should be considered. As shown in Fig. 19(a), the power consumption of the pump 1 is mainly influenced by the engine operating conditions. The power consumption of the pump 1 increases with the increment of engine speed and torque. This is due to the increase in the mass flow rate of the working fluid. The power consumption of the pump 1 is within the range of 0.07–1.93 kW, while the maximum back work ratio of the HT cycle can reach up to 12.79%. The power consumption of the pump 2 is presented in Fig. 19(b). It can be concluded that the power consumption of the pump 2 is obviously lower than that of the pump 1. The reason for this is that the enthalpy difference between the inlet and outlet of the pump at a lower pressure is small. Over the whole operating range, the power consumption of the pump 2 is within the range of 0.03–0.26 kW.

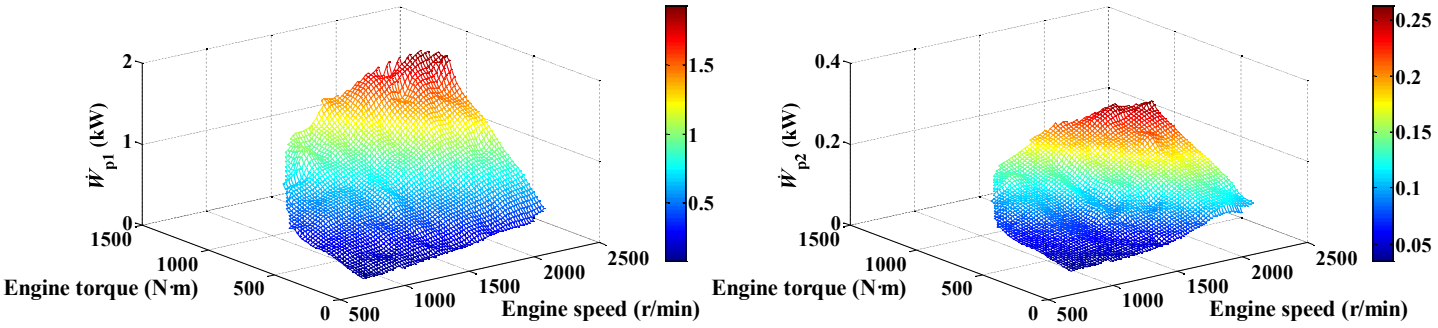

(a) Power consumption of the pump 1 (b) Power consumption of the pump 2

Fig. 19. Power consumptions of the pumps.

5.3. Heat transfer analysis of the dual loop ORC system

Fig. 20 shows the variation in the total waste heat recovered from the CNG engine and the heat transfer rate for each of the heat exchangers under various operating conditions. The variation in the total waste heat recovered from the CNG engine is presented in Fig. 7(a). As shown in Fig. 1, the total waste heat recovered from the CNG engine includes the exhaust energy, the waste heat of the coolant, and released heat from the turbocharged air in the intercooler. The total waste heat recovered from the CNG engine increases with engine speed and torque, and its value is within the range of 21.04–237.33 kW over the whole operating range. Fig. 20(b) shows the variation in the heat transfer rate of evaporator 1 under various operating conditions. The heat transfer rate of evaporator 1 also increases with engine speed and torque. Compared with Figs. 18(a) and (b), the exhaust energy significantly influences the net power output and the mass flow rate of the ORC system. The heat transfer rate of the evaporator 1 is within the range of 7.07–168.19 kW over the whole operating range. Fig. 20(c) shows the variation in the heat transfer rate of the intercooler under various operating conditions. Combined with Fig. 7, this figure indicates that the released heat from the turbocharged air in the intercooler increases with engine speed and torque. The heat transfer rate of the intercooler also increases. The heat transfer rate of the intercooler is within the

range of 0.02–26.03 kW over the whole operating range of the CNG engine. Fig. 20(d) shows the variation in the heat transfer rate of the preheater with the engine operating conditions. As shown in Figs. 1 and 3, the preheater is a coupling unit between the HT cycle and LT cycle. The heat transfer rate of the preheater increases with engine speed and torque, the values of which are within the range of 3.28–77.85 kW. Fig. 20(e) shows the variation in the heat transfer rate of evaporator 2 under various operating conditions. The heat transfer rate of the evaporator 2 is mainly influenced by engine speed. Compared with Fig. 8(d), a similar trend is observed in the heat transfer rate of evaporator 2 and the waste heat of the coolant. The heat transfer rate of the evaporator 2 is within the range of 13.95–44.35 kW over the whole operating range of the CNG engine. Fig. 20(f) shows the variation in the heat transfer rate of the condenser under various operating conditions. As a heat rejection unit of the ORC system, the heat transfer rate of the condenser also increases with engine speed and torque. The heat transfer rate of the condenser is within the range of 15.91–136.15 kW.

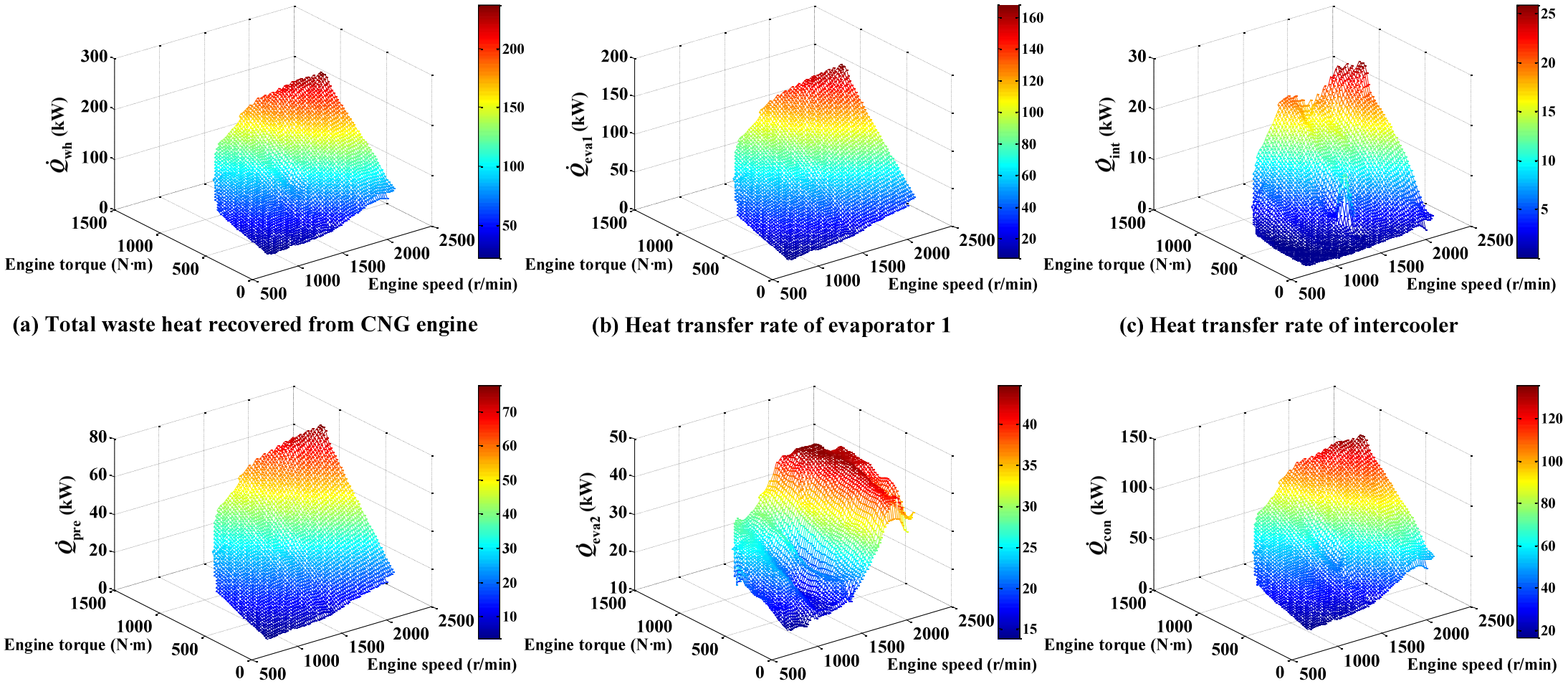

Fig. 20. Variation of the total waste heat recovered from the CNG engine and the heat transfer rate for each of the heat exchangers.

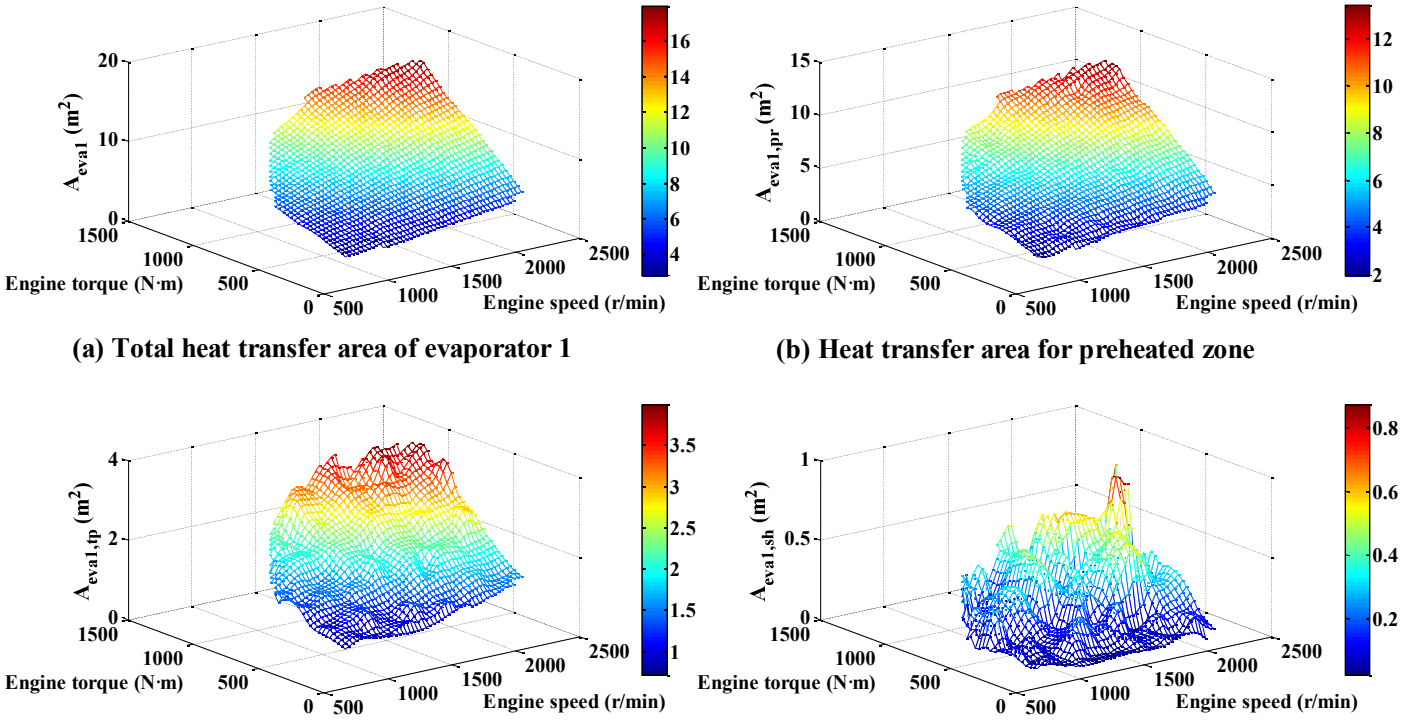

Fig. 21. Variation of the heat transfer area of evaporator 1.

Fig. 21 shows the variation in the heat transfer area of evaporator 1 under various operating conditions. The variation in the total heat transfer area of evaporator 1 with the engine operating conditions is presented in Fig. 21(a). The total heat transfer area is mainly influenced by the engine operating conditions, and increases with engine speed and torque. The total heat transfer area of evaporator 1 is within the range of 2.64–18.13 m^2 over the whole operating range of the CNG engine. Figs. 21(b)–(d) show the variation in the heat transfer area for the preheated zone, evaporation zone, and superheated zone, respectively. The preheated zone has the maximum heat transfer area, followed by the evaporation zone, and finally, the superheated zone. The heat transfer area of the preheated zone accounts for nearly 75% of the total heat transfer area under most operating conditions. This phenomenon is mainly attributed to the difference in the heat transfer rate for each zone. As shown in Figs. 16(a)–(c), the HT cycle has a high evaporation pressure and a low

superheat degree, and the condensation temperature is close to its lower bound. When the condensation temperature of the HT cycle is kept constant, the enthalpy difference of the preheated zone increases with evaporation pressure, whereas the enthalpy difference of the evaporation zone decreases with increasing evaporation pressure. Furthermore, the enthalpy difference of the superheated zone is mainly influenced by the superheat degree. When the mass flow rate of the working fluid is certain, the heat transfer rate for each zone is determined by the enthalpy difference.

From Fig. 21(b), the heat transfer area of the preheated zone increases with engine speed and torque. As shown in Fig. 6(c), the exhaust temperature increases with increasing engine speed and torque. By contrast, the condensation temperature of the HT cycle and the exhaust temperature at the outlet of evaporator 1 are kept nearly constant, which will result in a decrease in the logarithmic mean temperature difference of the preheated zone. Simultaneously, the increase in the heat transfer coefficient is lower than that in the heat transfer rate. Therefore, the heat transfer area of the preheated zone is mainly influenced by the engine operating conditions. The heat transfer area of the preheated zone is within the range of 1.92–13.37 m^2 over the whole operating range of the CNG engine. Fig. 21(c) shows the variation in the heat transfer area of the evaporation zone under various operating conditions. Similar to the preheated zone, the heat transfer area of the evaporation zone also increases with engine speed and torque. This phenomenon is attributed to the increase of the logarithmic mean temperature difference and the heat transfer coefficient with engine speed and torque, whereas the heat transfer rate has a larger increment, thereby resulting in an increase in the heat transfer area. The heat transfer area of the evaporation zone is within the range of 0.67–4.07 m^2

over the whole operating range. Fig. 21(d) shows the variation in the heat transfer area of the superheated zone under various operating conditions. The heat transfer area of the superheated zone varies within a small range with the engine operating conditions. As shown in Fig. 6(c), the exhaust temperature increases with engine speed and torque, which results in an increase in the logarithmic mean temperature difference and the heat transfer coefficient. The heat transfer area of the superheated zone is within the range of 0.02–0.9 m^2.

Fig. 22 shows the variation in the heat transfer area for the LT cycle under various operating conditions. The variation in the heat transfer area of the intercooler is presented in Fig. 22(a). The heat transfer area of the intercooler is mainly influenced by engine speed. When the CNG engine operates under medium speed regions, the intercooler has the maximum heat transfer area. This phenomenon is attributed to the decrease in the logarithmic mean temperature difference. As shown in Fig. 7(b), the turbocharged air temperature at the outlet of the intercooler is mainly determined by engine speed. When the CNG engine operates under low and high speed regions, the intake air temperature at the outlet of the intercooler is relatively high. By contrast, the turbocharged air temperature at the outlet of the intercooler is relatively low under medium speed regions. Therefore, the heat transfer coefficient is low under medium speed regions, which results in a high heat transfer area. When the CNG engine operates under low and high speed regions, the logarithmic mean temperature difference and the heat transfer coefficient vary within a small range. The heat transfer area is mainly influenced by the intercooler heat rejection. The heat transfer area of the intercooler is within the range of 0.08–1.11 m^2 over the whole operating range of the CNG engine. Fig. 22(b) shows the variation in the heat transfer area of the preheater with engine operating

conditions. The heat transfer area of the preheater is mainly determined by the engine operating conditions. It increases with engine speed and torque. As shown in Figs. 16(c) and (d), the condensation temperature of the HT cycle and the evaporation temperature of the LT cycle are kept nearly constant over the whole operating range of the CNG engine. Consequently, the logarithmic mean temperature difference and the heat transfer coefficient are slightly influenced by the engine operating conditions. The heat transfer area is determined by the heat transfer rate. The heat transfer area of the preheater is within the range of 0.03–1.69 m^2. Fig. 22(c) shows the variation in the heat transfer area of evaporator 2 under various operating conditions. The heat transfer area of evaporator 2 is mainly influenced by engine speed. As shown in Figs. 8(a), (b), and 16(d), the coolant temperature at the outlet of the CNG engine and the evaporation temperature of the LT cycle vary within a small range. Therefore, the heat transfer area is closely related to the heat transfer rate. By contrast, the waste heat of the coolant increases with engine speed. The heat transfer area of the evaporator 2 is within the range of 0.12–0.63 m^2 over the whole operating range of the CNG engine. Fig. 22(d) shows the variation in the heat transfer area of the condenser under various operating conditions. As shown in Fig. 16(e), the condensation temperature of the LT cycle is kept nearly constant over the whole operating range. Similar to the preheater and evaporator 2, the logarithmic mean temperature difference and the heat transfer coefficient of the condenser are slightly influenced by engine operating conditions. The heat transfer area is determined by the heat transfer rate. As shown in Fig. 20(f), the heat transfer rate of the condenser increases with engine speed and torque. The heat transfer area of the condenser is within the range of 0.86–4.48 m^2.

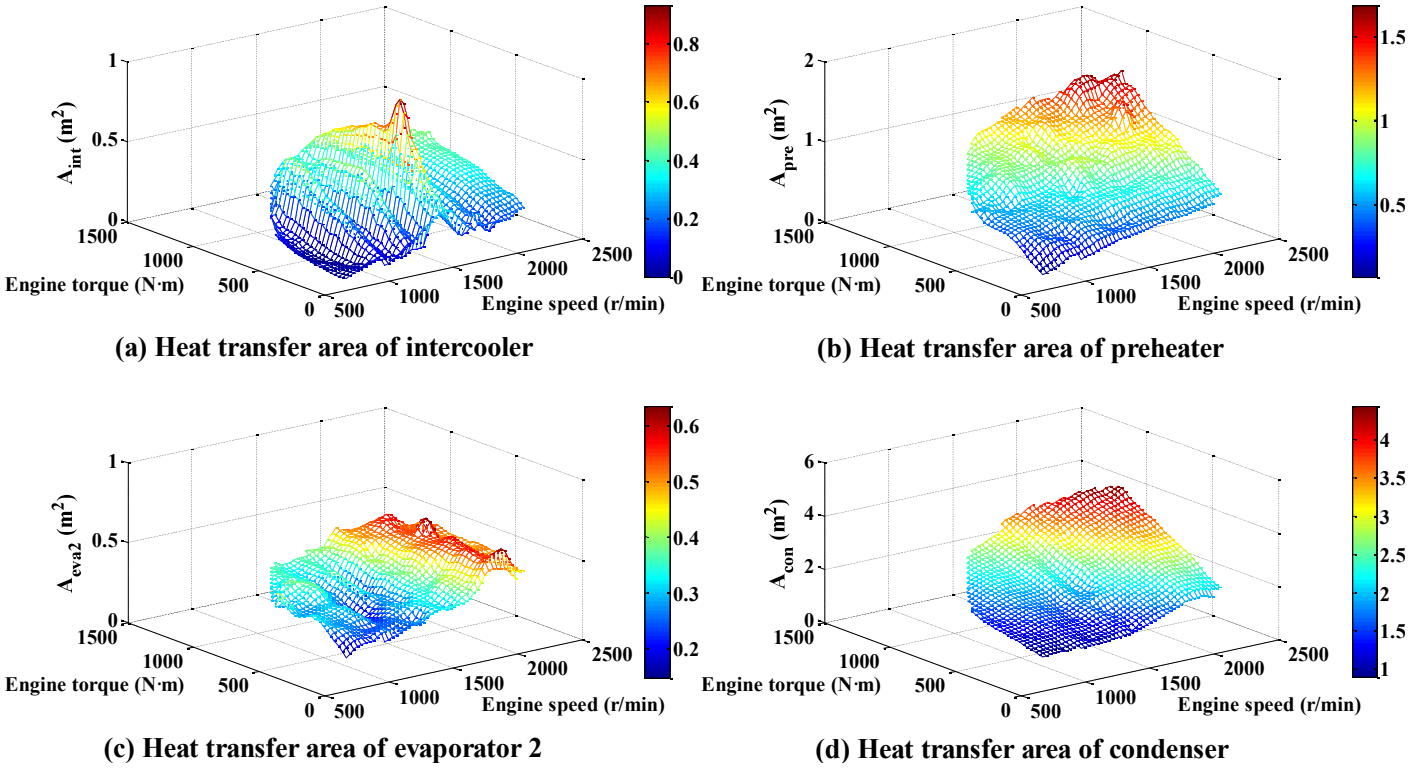

Fig. 22. Variation of the heat transfer area for the LT cycle.

From the aforementioned analysis, the heat exchanger, which is a coupling unit in thermal systems, plays an important role. When selecting the appropriate type of heat exchanger in waste heat recovery applications for IC engines, two issues should be addressed. First, the exhaust temperature of the CNG engine is over 800 K at most operating conditions. Therefore, the heat exchanger used for recovering the exhaust waste heat must operate normally under high temperature conditions. Fin-and-tube and brazed plate heat exchangers are generally suited for high-temperature and high-pressure applications. Second, the installation space should be considered when applying a waste heat recovery system to a vehicle engine. Under the same heat load condition, the smaller the installation space is, the better the performance of the heat exchanger. A comparison between Figs. 21 and 22 indicates that the plate heat exchanger has a smaller heat transfer area than the fin-and-tube heat exchanger. Another type of plate heat exchanger is the gasketed plate and frame

heat exchanger, whose operating temperature is typically below 500 K because of the limitation of the gasket. One of the advantages of using this type of heat exchanger is the capability to adjust its thermal performance by adding or removing plates. Therefore, the gasketed plate and the frame heat exchanger are recommended for the LT cycle. In this study, the multi-objective optimization aims to obtain the optimal operating regions of the dual loop ORC system by considering thermodynamic performance and heat transfer characteristics. To perform a comprehensive evaluation of the optimization results, Fig. 23 provides the comparison between the original and the optimized results in terms of the external characteristics of the CNG engine. For the original results, the decision variables are set equal to the median value of the logical bounds. The optimized results are clearly better than the original results from the thermodynamic point of view. Using Fig. 23(a) as an example, the net power output of the HT cycle after optimization is higher than its original value. Furthermore, the difference between the original and the optimized results is widened when the engine speed is increased. Overall, the multi-objective optimization method adopted in this study positively affects the dual loop ORC system. By contrast, a comparison with similar studies is indispensable to evaluate the optimal performances of the dual loop ORC system under different heat source conditions. A review of the applications of the dual loop ORC system in IC engines is presented in Table 7. No discernible difference is generally observed between a diesel engine and other types of engine for waste heat recovery. IC engines act just as the waste heat source for the ORC system. As shown in Table 7, the thermodynamic performance of the dual loop ORC mainly depends on the power output of the IC engines. The net power output of the dual loop ORC system varies from 9.57–39.67 kW, whereas the thermal efficiency is approximately 10%. The results

presented in this study are consistent with the results presented in Table 1 because since an increment in the engine power output causes an increase in the net power output of the dual loop ORC system.

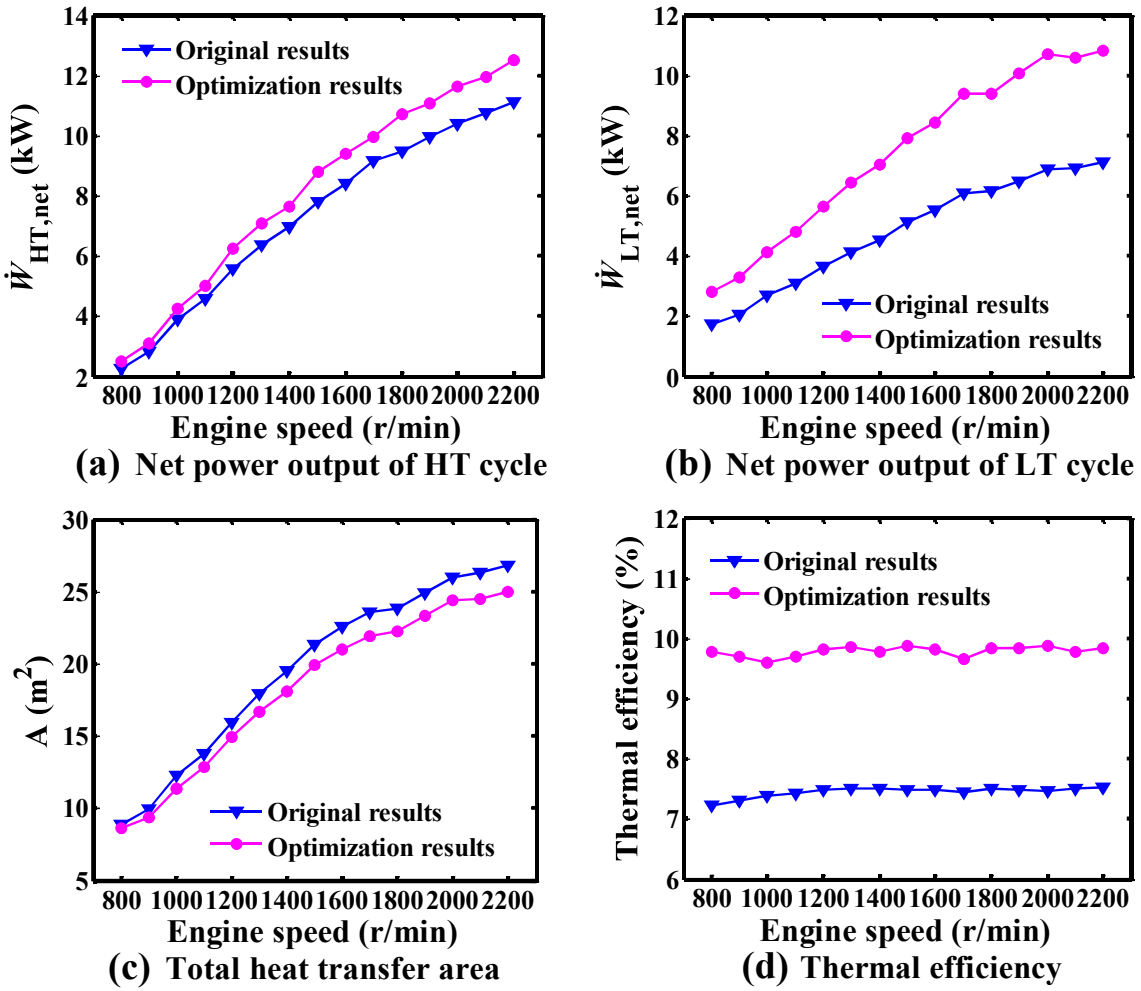

Fig. 23. Comparison between original and optimizaiton results at external characteristics of the CNG engine.

Table 7 Review of application of dual loop ORC system in IC engines.

Fuel	Engine specifications	Heat source	Configuration types	Optimal performances	Refs.
Gasoline	Displacement: 1.793 L Cylinder number: 4 Rated power: 130 kW	Exhaust gas and coolant	Dual loop ORC system	$\dot{W}_{HT,net}$ =9.57 kW $\dot{W}_{LT,net}$ =26.39 kW	Wang et al. [20]
Diesel	Displacement: 11.596 L Cylinder number: 6 Rated power: 247 kW	Exhaust gas, intake air and coolant	Dual loop ORC system HT cycle contains an IHE	$\dot{W}_{tot,net}$ =27.85 kW η_{WHRE} =5.4%	Yang et al. [21]
Diesel	Rated power: 235.8 kW Engine efficiency: 41.81%	Exhaust gas and coolant	Regenerative dual loop ORC system	$\dot{W}_{tot,net}$ =39.67 kW	Shu et al. [22]
Diesel	Displacement: 2.499 L Cylinder number: 4 Rated power: 105 kW	Exhaust gas, intake air and coolant	Dual loop ORC system	$\dot{W}_{tot,net}$ =18.89 kW	Zhang et al. [23]
Diesel	Displacement: 8.424 L Cylinder number: 6 Rated power: 243 kW	Exhaust gas, exhaust gas recirculation, intake air and coolant	Cascade-ORC system	$\dot{W}_{tot,net}$ =33.9 kW η_{th} =9.9%	Shu et al. [24]
Diesel	Displacement: 2.499 L Cylinder number: 4 Rated power: 235.8 kW	Exhaust gas and coolant	Dual loop ORC system	$\dot{W}_{tot,net}$ =36.77 kW	Shu et al. [30]

Generally speaking, the heat exchanger is a fixed size, and most of the heat exchangers operate under stable conditions. However, the waste heat characteristics of the IC engines and operating parameters of the ORC system will vary with the operating conditions, thus affecting the thermodynamic properties of the working fluid. So the effective heat transfer area is variable under various operating conditions of the IC engines. The corresponding optimal heat transfer area is based on an actual model. It is essential to pick a size and assess the performance impacts of the fixed size on the operation at off design conditions. More detailed discussion on this topic will be finished in future work.

6. **Conclusions**

In this study, a dual loop ORC system is adopted to recover exhaust energy, waste heat from the coolant system, and rejected heat from the intercooler of a six-cylinder CNG engine. The thermodynamic, heat transfer, and optimization models for the dual loop ORC system are established. On the basis of the waste heat characteristics of the CNG engine over the whole operating range, genetic algorithm is used to solve the Pareto solution of the thermodynamic and heat transfer performances to maximize the net power output and minimize the heat transfer area. Combined with the optimization results, the optimal parameter regions of the dual loop ORC system are determined under various operating conditions, and the variation in the heat transfer area with the conditions of the CNG engine is analyzed. The main conclusions can be summarized as follows:

(1) The optimal evaporation pressure of the HT cycle is higher than 2.2 MPa over the whole operating range of the CNG engine. Under most operating conditions, the optimal evaporation

pressure of the HT cycle is within the range of 2.5–2.9 MPa. The optimal superheat degree is mainly influenced by the engine operating conditions. Its value ranges from 0.43–12.35 K. The optimal condensation temperature of the HT cycle is kept nearly constant at 350.15 K.

(2) The optimal evaporation temperature of the LT cycle is within the range of 339–343.15 K. It increases with decreasing engine torque. The optimal condensation temperature of the LT cycle is kept nearly constant at 298.15 K. The optimal exhaust temperature at the outlet of evaporator 1 varies within a small range. Its value is kept nearly constant at 423.15 K under most operating conditions.

(3) The net power output and mass flow rate of the working fluid for the HT and LT cycles are determined by the operating conditions of the CNG engine. The net power output of the HT cycle is within the range of 0.49–12.56 kW, whereas the LT cycle is within the range of 1.35–11.06 kW. Furthermore, the thermal efficiency of the dual loop ORC system ranges from 8.79%–10.17%.

(4) The heat transfer area for each heat exchanger is mainly influenced by the engine operating conditions and the operating parameters of the dual loop ORC system. In the HT cycle, the preheated zone of evaporator 1 has the maximum heat transfer area. Under most operating conditions, the heat transfer area of the preheated zone accounts for nearly 75% of the total heat transfer area.

(5) In the dual loop ORC system, the heat transfer area of the plate heat exchanger is evidently lower than that of the fin-and-tube heat exchanger. Under the rated condition of the CNG engine, the heat transfer areas of evaporator 1, the intercooler, the preheater, evaporator 2, and

the condenser are 18.13 m^2, 1.11 m^2, 1.69 m^2, 0.63 m^2, and 4.48 m^2, respectively.

This paper only presents an analysis of the dual loop ORC system for CNG engine waste heat recovery. The methods and discussions of this paper are helpful to optimize the vapor power cycles for the purpose of waste heat recovery of IC engines. It is a very meaningful work to generalize a commonly used method to any combinations of heat engines and heat recovery systems. That will be part of authors' future work.

Acknowledgments

This work was sponsored by the Projects of International Cooperation and Exchanges NSFC (Grant No. 51611130193), the National Natural Science Foundation of China (Grant No. 51376011), the Beijing Natural Science Foundation Program (Grant No. 3152005), the National Basic Research Program of China (973 Program) (Grant No. 2013CB228306), and the Scientific Research Key Program of Beijing Municipal Commission of Education (Grant No. KZ201410005003). The authors would like to thank the reviewers for their valuable comments on this research.

References

[1] Huang B, Hu EJ, Huang ZH, Zheng JJ, Liu B, Jiang DM. Cycle-by-cycle variations in a spark ignition engine fueled with natural gas–hydrogen blends combined with EGR. Int J Hydrogen Energy 2009;34:8405–14.

[2] Wang TY, Zhang YJ, Peng ZJ, Shu GQ. A review of researches on thermal exhaust heat recovery with Rankine cycle. Renew Sustain Energy Rev 2011; 15:2862–71.

[3] Tian H, Shu GQ, Wei HQ, Liang XY, Liu LN. Fluids and parameters optimization for the

organic Rankine cycles (ORCs) used in exhaust heat recovery of Internal Combustion Engine (ICE). Energy 2012;47:125–36.

[4] Xu JL, Yu C. Critical temperature criterion for selection of working fluids for subcritical pressure Organic Rankine cycles. Energy 2014;74:719–33.

[5] Yang FB, Zhang HG, Bei C, Song SS, Wang EH. Parametric optimization and performance analysis of ORC (organic Rankine cycle) for diesel engine waste heat recovery with a fin-and-tube evaporator. Energy 2015;91:128–41.

[6] Quoilin S, Broek MVD, Declaye S, Dewallef P, Lemort V. Techno-economic survey of Organic Rankine Cycle (ORC) systems. Renew Sustain Energy Rev 2013;22:168–86.

[7] Lodwig E. Performance of a 35 HP organic Rankine cycle exhaust gas powered system. 1970. SAE Paper 700160.

[8] Leising CJ, Purohit GP, DeGrey SP, Finegold JG. Waste heat recovery in truck engines. 1978. SAE Paper 780686.

[9] Doyle E, Dinanno L, Kramer S. Installation of a diesel-organic Rankine compound engine in a class 8 truck for a single vehicle test. 1979. SAE Paper 790646.

[10] Yu GP, Shu GQ, Tian H, Wei HQ, Liu LN. Simulation and thermodynamic analysis of a bottoming Organic Rankine Cycle (ORC) of diesel engine (DE). Energy 2013;51:281–90.

[11] Zhang J, Zhang HG, Yai K, Yang FB, Wang Z, Zhao GY, et al. Performance analysis of regenerative organic Rankine cycle (RORC) using the pure working fluid and the zeotropic mixture over the whole operating range of a diesel engine. Energy Convers Manag 2014;84:282–94.

[12] Yue C, Han D, Pu WH, He WF. Energetic analysis of a novel vehicle power and cooling/heating cogeneration energy system using cascade cycles. Energy 2015;82:242–55.

[13] Galindo J, Ruiz S, Dolz V, Royo-Pascual L, Haller R, Nicolas B, et al. Experimental and thermodynamic analysis of a bottoming Organic Rankine Cycle (ORC) of gasoline engine using swash-plate expander. Energy Convers Manag 2015;103:519–32.

[14] Yang FB, Zhang HG, Song SS, Bei C, Wang HJ, Wang EH. Thermoeconomic multi-objective optimization of an organic Rankine cycle for exhaust waste heat recovery of a diesel engine. Energy 2015;93:2208–28.

[15] Liu W, Meinel D, Gleinser M, Wieland C, Spliethoff H. Optimal Heat Source Temperature for thermodynamic optimization of sub-critical Organic Rankine Cycles. Energy 2015;88:897–906.

[16] Yang XF, Xu JL, Miao Z, Zou JH, Yu C. Operation of an organic Rankine cycle dependent on pumping flow rates and expander torques. Energy 2015;90:864–78.

[17] Vaja I, Gambarotta A. Internal Combustion Engine (ICE) bottoming with Organic Rankine Cycles (ORCs). Energy 2010;35:1084–93.

[18] Srinivasan KK, Mago PJ, Krishnan SR. Analysis of exhaust waste heat recovery from a dual fuel low temperature combustion engine using an Organic Rankine Cycle. Energy 2010;35:2387–99.

[19] Usman M, Imran M, Yang Y, Park BS. Impact of organic Rankine cycle system installation on light duty vehicle considering both positive and negative aspects. Energy Convers Manag 2016;112:382–94.

[20] Wang EH, Zhang HG, Zhao Y, Fan BY, Wu YT, Mu QH. Performance analysis of a novel

system combining a dual loop organic Rankine cycle (ORC) with a gasoline engine. Energy 2012;43:385–95.

[21] Yang FB, Dong XR, Zhang HG, Wang Z, Yang K, Zhang J, Wang EH, Liu H, Zhao GY. Performance analysis of waste heat recovery with a dual loop organic Rankine cycle (ORC) system for diesel engine under various operating conditions. Energy Convers Manag 2014;80:243–55.

[22] Shu GQ, Liu LN, Tian H, Wei HQ, Liang YC. Analysis of regenerative dual-loop organic Rankine cycles (DORCs) used in engine waste heat recovery. Energy Convers Manag 2013;76:234–43.

[23] Zhang HG, Wang EH, Fan BY. A performance analysis of a novel system of a dual loop bottoming organic Rankine cycle (ORC) with a light-duty diesel engine. Appl Energy 2013;102:1504–13.

[24] Shu GQ, Yu GP, Tian H, Wei HQ, Liang XY, Huang ZY. Multi-approach evaluations of a cascade-Organic Rankine Cycle (C-ORC) system driven by diesel engine waste heat: Part A – Thermodynamic evaluations. Energy Convers Manag 2016;108:579–95.

[25] Song J, Gu CW. Parametric analysis of a dual loop Organic Rankine Cycle (ORC) system for engine waste heat recovery. Energy Convers Manag 2015;105:995–1005.

[26] Wang EH, Zhang HG, Fan BY, Wu YT. Optimized performances comparison of organic Rankine cycles for low grade waste heat recovery. J Mech Sci Technol 2012;26:2301–12.

[27] Xi H, Li MJ, Xu C, He YL. Parametric optimization of regenerative organic Rankine cycle (ORC) for low grade waste heat recovery using genetic algorithm. Energy 2013;58:473–82.

[28] Wang JF, Yan ZQ, Wang M, Ma SL, Dai YP. Thermodynamic analysis and optimization of an (organic Rankine cycle) ORC using low grade heat source. Energy 2013;49:356–65.

[29] Wang EH, Zhang HG, Fan BY, Ouyang MG, Yang FY, Yang K, et al. Parametric analysis of a dual-loop ORC system for waste heat recovery of a diesel engine. Appl Therm Eng 2014;67:168–78.

[30] Shu GQ, Liu LN, Tian H, Wei HQ, Yu GP. Parametric and working fluid analysis of a dual-loop organic Rankine cycle (DORC) used in engine waste heat recovery. Appl Energy 2014;113:1188–98.

[31] Wang EH, Zhang HG, Fan BY, Ouyang MG, Yang K, Yang FY, et al. 3D numerical analysis of exhaust flow inside a fin-and-tube evaporator used in engine waste heat recovery. Energy 2015;82:800–12.

[32] Imran M, Usman M, Park BS, Kim HJ, Lee DH. Multi-objective optimization of evaporator of organic Rankine cycle (ORC) for low temperature geothermal heat source. Appl Therm Eng 2015;80:1–9.

[33] Bei C, Zhang HG, Yang FB, Song SS, Wang EH, Liu H, et al. Performance Analysis of an Evaporator for a Diesel Engine–Organic Rankine Cycle (ORC) Combined System and Influence of Pressure Drop on the Diesel Engine Operating Characteristics. Energies 2015;8:5488–515.

[34] Papadopoulos AI, Stijepovic M, Linke P. On the systematic design and selection of optimal working fluids for Organic Rankine Cycles. Appl Therm Eng 2010;30:760–9.

[35] Yu HS, Feng X, Wang YF. A new pinch based method for simultaneous selection of working

fluid and operating conditions in an ORC (Organic Rankine Cycle) recovering waste heat. Energy 2015;90:36–46.

[36] Wang EH, Zhang HG, Fan BY, Ouyang MG, Zhao Y, Mu QH. Study of working fluid selection of organic Rankine cycle (ORC) for engine waste heat recovery. Energy 2011;36:3406–18.

[37] Mago PJ, Luck P. Evaluation of the potential use of a combined micro-turbine organic Rankine cycle for different geographic locations. Appl Energy 2013;102:1324–33.

[38] Heywood JB. Internal combustion engine fundamentals. New York: McGraw–Hill; 1988.

[39] Zukauskas A. 1972. Heat transfer from tubes in cross flow. Adv. Heat Transfer. New York: Academic Press, 1972: 93–106.

[40] Gnielinski V. New equations for heat mass transfer in turbulent pipe and channel flows. Int Chem Eng 1976; 16: 359–68.

[41] Wang JF, Yan ZQ, Wang M, Li MQ, Dai YP. Multi-objective optimization of an organic Rankine cycle (ORC) for low grade waste heat recovery using evolutionary algorithm. Energy Convers Manag 2013;71:146–58.

[42] Liu Z, Winterton RHS. A general correlation for saturated and subcooled flow boiling in tubes and annuli, based on a nucleate pool boiling equation. Int J Heat Mass Tran 1991;34(11):2759–66.

[43] García-Cascales JR, Vera-García F, Corberán-Salvador JM, Gonzálvez-Maciá J. Assessment of boiling and condensation heat transfer correlations in the modelling of plate heat exchangers. Int J Refrig 2007;30:1029–41.

[44] Yan YY, Lio HC, Lin TF. Condensation heat transfer and pressure drop of refrigerant R-134a in

a plate heat exchanger. Int J Heat Mass Tran 1999;42:993–1006.

[45] Yan YY, Lin TF. Evaporation heat transfer and pressure drop of refrigerant R- 134a in a plate heat exchanger. J Heat Trans-T ASME 1999;121:118–27.

[46] Matlab, Global Optimization Toolbox User's Guide, Matlab R2010a, The MathWorks, Inc, 2010.

[47] Balachandran M, Gero JS. A comparison of three methods for generating the Pareto optimal set. Eng Optimiz 1984; 7 (4): 319–36.

[48] Wikipedia: Multi-objective optimization. <https://en.wikipedia.org/wiki/Multi-objective _optimization> [accessed on August 15, 2016].

[49] Sayyaadi H, Mehrabipour R. Efficiency enhancement of a gas turbine cycle using an optimized tubular recuperative heat exchanger. Energy 2012;38:362–75.

[50] Sanaye S, Sarrafi A. Optimization of combined cooling, heating and power generation by a solar system. Renew Energy 2015;80:699–712.

[51] Haghighat Mamaghani A, Najafi B, Shirazi A, Rinaldi F. 4E analysis and multi-objective optimization of an integrated MCFC (molten carbonate fuel cell) and ORC (organic Rankine cycle) system. Energy 2015;82:650–63.